Journal of Structural Geology 37 (2012) 200–222

Contents lists available at SciVerse ScienceDirect

Journal of Structural Geology

journal homepage: www.elsevier.com/locate/jsg

Rheological constraints on quartz derived from scaling relationships and numerical models of sheared brittle-ductile quartz veins, central Southern Alps, New Zealand

Susanne Grigull [a,e,*], Susan M. Ellis [b], Timothy A. Little [a], Matthew P. Hill [a,c], Susanne J.H. Buiter [d]

[a] School of Geography, Environment and Earth Sciences, Victoria University of Wellington, PO Box 600, Wellington 6140, New Zealand
[b] GNS Science, 1 Fairway Drive, PO Box 30368, Avalon, Lower Hutt 5010, New Zealand
[c] School of Earth and Environment, University of Western Australia, 35 Stirling Highway, Crawley, WA 6009, Australia
[d] Centre for Geodynamics, Geological Survey of Norway, Leiv Eirikssons vei 39, 7491 Trondheim, Norway
[e] Ruhr-University Bochum, Department of Geology, Mineralogy and Geophysics, Universitätsstr. 150, 44780 Bochum, Germany

ARTICLE INFO

Article history:
Received 7 April 2011
Received in revised form
16 January 2012
Accepted 18 January 2012
Available online 1 February 2012

Keywords:
Quartz
Rheology
Flow law
Brittle-ductile
Shear zone
Numerical modelling

ABSTRACT

The mechanical properties of quartz strongly influence the strength of continental crust, but natural examples to constrain quartz rheology are rare. Here, brittle-ductile fault arrays in the Southern Alps, New Zealand, provide a natural laboratory into the rheology of quartz rocks. The faults formed in the hanging wall of the Alpine Fault during the late Cenozoic at ≥21 km depth. They are near-vertical, extend over tens of metres, strike sub-parallel to the Alpine Fault, and displace quartzofeldspathic meta-greywacke through predominantly brittle processes. They also displace centimetre-thick quartz veins that are discordant to the dominant schist foliation with variably ductile to brittle slip. We use field-observed geometrical scaling relationships related to the sheared quartz veins and interactions between brittle faults and ductilely deforming quartz veins that intersect them to produce a set of viable numerical models. Quartz rheology is modelled by linear or power law creep, and the material parameters extracted for the quartz veins, together with viscous and brittle strength ratios between vein quartz and schist. The results indicate that under the prevailing deformation conditions, the dominant deformation mechanism in the quartz veins was dislocation creep resulting in a non-linear quartz rheology.

1. Introduction

Quartz is one of the most abundant minerals in the continental crust, and the rheology of quartz-dominated rocks is thought to be the main control on the depth of the brittle-ductile[1] transition and the nucleation depth of major earthquakes (e.g., Scholz, 1988). However, we know little about the actual rheology of quartz under geological conditions near the brittle to ductile transition. Most knowledge of the ductile behaviour of quartz is based on laboratory experiments conducted under unnaturally hot and fast deformation conditions, i.e., at temperatures of > 700 °C and strain rates in the order of 10^{-7}–10^{-4} s^{-1} (e.g., Hirth and Tullis, 1992; Paterson and Luan, 1990; Luan and Paterson, 1992; Gleason and Tullis, 1995; Rutter and Brodie, 2004a, 2004b). Flow laws for quartz that are derived in the laboratory are of the form

$$\dot{\varepsilon} = A_E \cdot \sigma_d^n \cdot f_{H_2O}^m \cdot d^{-r} \cdot \exp\left(-Q/RT\right) \quad (1)$$

where $\dot{\varepsilon}$ is the uniaxial or triaxial strain rate in [s^{-1}], A_E is the experimentally derived pre-exponential factor with units [MPa^{-n-m} s^{-1} μm^r], σ_d is the differential stress in [MPa], n is the stress exponent, f_{H_2O} is water fugacity in [MPa], m is the water fugacity exponent, d is grain size in [μm], r is the grain size exponent, Q is activation enthalpy with units of [J mol^{-1}], R = 8.314 J mol^{-1} K^{-1} is the universal gas constant, and T is temperature in [K]. For a grain size exponent $r = 0$ and a stress exponent $n \geq 2$, Eq. (1) describes typical grain size insensitive dislocation creep behaviour. For a grain-size exponent $r \geq 1$ and a stress exponent $n < 2$, the flow law becomes grain size dependent

* Corresponding author. Ruhr-University Bochum, Department of Geology, Mineralogy and Geophysics, Universitätsstr. 150, 44780 Bochum, Germany. Tel.: +49 234 32 23232.
E-mail addresses: Susanne.Grigull@rub.de, sannegri@googlemail.com (S. Grigull), S.Ellis@gns.cri.nz (S.M. Ellis), Tim.Little@vuw.ac.nz (T.A. Little), matt@mhgeol.com (M.P. Hill), Susanne.Buiter@ngu.no (S.J.H. Buiter).

[1] In this paper we use the term 'ductile' in a similar way to Fusseis et al. (2006), i.e., as a synonym to 'solid-state viscous'. However, we kept in mind that 'ductility' is merely a description of distributed coherent deformation and does not describe a 'mechanistic concept'. Similarly, we use the term "brittle" to refer to pressure-sensitive frictional plasticity throughout the paper.

0191-8141/$ – see front matter © 2012 Elsevier Ltd. All rights reserved.
doi:10.1016/j.jsg.2012.01.006

and deformation is accommodated by diffusional processes. A key question is whether one can reliably extrapolate such experimentally derived flow laws for quartz to natural geological conditions.

Some field observations have been used to test the experimentally derived flow laws for quartz and quartz-dominated rocks against natural examples (e.g., Kenis et al., 2004, 2005; Treagus, 1999; Hudleston and Lan, 1993, 1994, 1995; Lan and Hudleston, 1995a, 1995b, 1996; Talbot, 1999, 2001; Treagus and Treagus, 2002; Treagus et al., 1996; Treagus and Lan, 2000, 2003, 2004). Hirth et al. (2001) were able to obtain a quartzite flow law for rocks deformed in the Ruby Gap duplex, Australia (e.g., Dunlap et al., 1997), by comparing laboratory-derived microstructures to those found in naturally deformed rocks. Inferring grain size-insensitive deformation ($r = 0$), these authors predicted a value for the stress exponent of $n = 4$, a water fugacity exponent of $m = 1$, and $A_E = 10^{-11.2 \pm 0.2}$ MPa^{-n-m} s^{-1}.

The above examples assume that both quartz and matrix are deforming viscously. However, many field examples of deformed rocks display a mixture of brittle, semi-brittle, and viscous behaviour. Only a few studies have investigated this type of behaviour; Mancktelow and Pennacchioni (2005) describe the role of precursory brittle faults on the development of ductile shear zones; and Fusseis et al. (2006) the interactions and networking of brittle to ductile shear zones. Numerical modelling by Schueller et al. (2005) investigates brittle-viscous coupling of linear viscous layers surrounding a strain softening brittle material.

In this paper we attempt to extract information about quartz rheology from field observations and computer modelling of variably brittlely to ductilely sheared quartz veins in the central Southern Alps, New Zealand. We also try to extract comparative rheological information about the psammitic and pelitic schists that host those quartz veins (Alpine Schist). Previous geological studies (e.g., Wightman, 2005; Wightman et al., 2006; Wightman and Little, 2007) provide useful constraints on the physical conditions during deformation (e.g., temperature). Because the fault array and veins occur in a well-constrained neotectonic context, the field site can be used as a natural laboratory of brittle-to-ductile quartz rheology in mid-crustal rocks. Constrained by the geologically determined physical conditions, and characteristic scaling relationships within and surrounding the veins, our finite element models attempt to replicate the sheared vein structures that we observed in the field. From the successful set of models, we estimate flow law parameters applicable to the deformed veins and quartzofeldspathic schist host, and thus assess whether laboratory-derived flow laws are applicable and relevant to naturally deforming quartz.

2. Tectonic setting and outcrop scale studies

2.1. The Southern Alps of New Zealand and the Alpine Fault

The Alpine Fault is the chief expression of the Pacific-Australian plate boundary on the South Island of New Zealand (Fig. 1a). During the past ~3 Myr relative plate motion between the two plates has been obliquely convergent at 37 ± 2 mm/yr at N71°E (averaged over 3 Ma; NUVEL-1A global plate motion model of De Mets et al., 1990, 1994). In the central Southern Alps, the dextral-reverse Alpine Fault has moved with a late Quaternary strike-slip rate of 23–25 mm/yr, and dip-slip rates of 8–12 mm/yr (Sutherland et al., 2006; Norris and Cooper, 2001, 2007) and has a surface dip of ~30–50° SE (e.g., Norris and Cooper, 1995; Kleffmann et al., 1998; Stern et al., 2007; Little et al., 2007; and references therein). Fault motion and accompanying erosion has exhumed Mesozoic quartzofeldspathic rocks (termed "Alpine Schist") in the hanging wall. Approximate mineral isograds plotted in Fig. 1b show that the metamorphic grade of the rocks to the east of the fault decreases from amphibolite facies adjacent to the mylonites of the Alpine Fault to prehnite-pumpellyite facies at the Main Divide 15–20 km

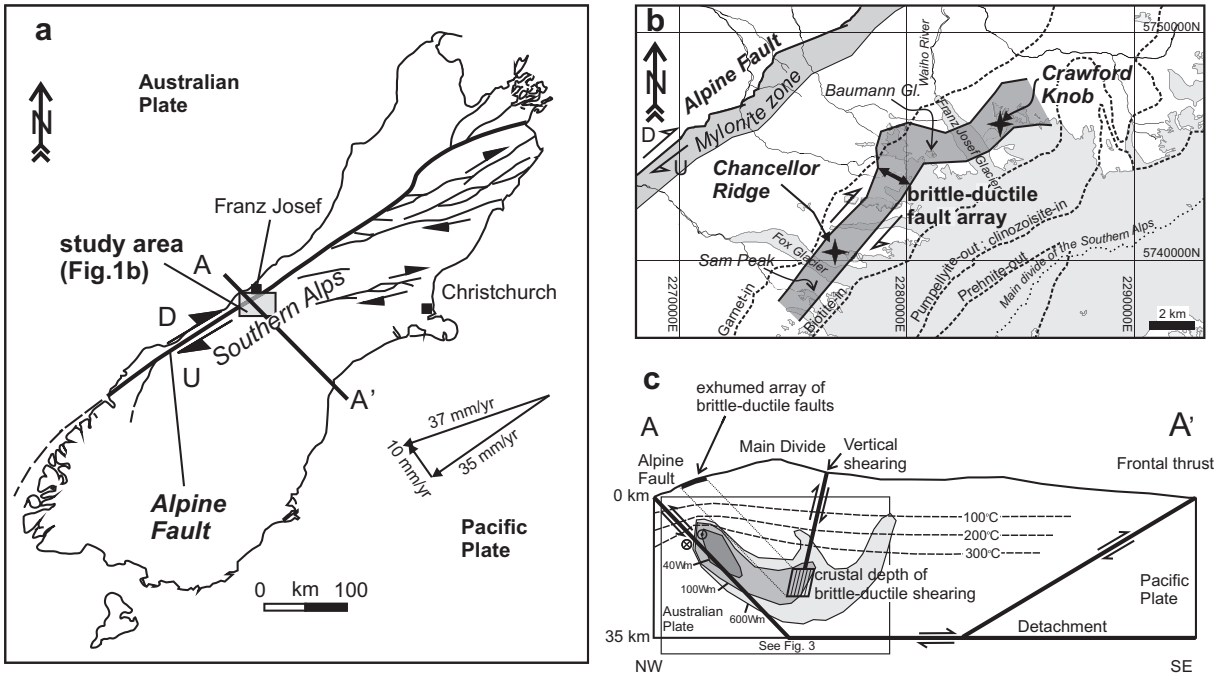

Fig. 1. Tectonic setting: a) South Island, New Zealand showing the dextral-reverse Alpine Fault with the fault trace trending 055°. Plate motion vectors are from NUVEL-1A model by De Mets et al. (1990, 1994). b) Aerial extent of the brittle-ductile fault array, its spatial relationship to the Alpine fault and the two main study locations Chancellor Ridge and Crawford Knob. Mineral isograds are taken from Cox and Barrell (2007). c) Schematic cross-section through the central Southern Alps after Wightman (2005). Superimposed grey shaded areas indicate low-resistivity zone imaged through geoelectric measurements by Wannamaker et al. (2002). Possible isotherm structure is after Batt and Braun (1999).

east of the Alpine Fault (Grapes and Watanabe, 1992; Cox and Barrell, 2007).

Stern et al. (2001, 2007; and references therein) were able to trace the Alpine Fault seismically to > 32 km depth. There, Stern et al. (2007) imaged sub-horizontal reflectors, interpreted as a detachment along which crustal rocks from greater than 25 km depth have been delaminated and transported onto the Alpine Fault (Fig. 1c). Stern et al. (2001, 2007) also describe a ~30 km-thick low-velocity zone in the hanging wall that extends to 35 km depth which they interpret as being due to interconnected metamorphic fluids, an interpretation supported by magnetotelluric measurements (Wannamaker et al., 2002), which showed a high conductivity region coinciding approximately with the low-velocity zone (resistivity contours in Fig. 1c). Vry et al. (2010) carried out mineral-equilibria modelling in an Alpine Schist metagreywacke sample. Their study predicts strong fluid production during shearing and exhumation of the quartzofeldspathic rocks which may explain the low-resistivity, low-velocity zone mentioned above.

2.2. Study area: an array of brittle-ductile faults

In the central part of the Southern Alps near Franz Josef Glacier (Fig. 1a), a 1–2 km wide array of discrete, planar, closely spaced, near-vertical, brittle-ductile faults is found in the uplifted hanging wall of the Alpine Fault (Fig. 1b, c). The fault array is located 5–7 km structurally above the Alpine Fault, corresponding to the distance today of the array normal to the Alpine Fault, assuming no volume loss or viscous deformation at the base. The field data for this paper were derived from glacially scoured outcrops at two locations in this array: Chancellor Ridge and Crawford Knob (Fig. 1b).

In the field area, Alpine Schist consists mainly of biotite-grade quartzofeldspathic psammopelitic metagreywacke. The neotectonic fault array cuts and offsets the foliation in this schist at an acute angle and also truncates pre-existing quartz veins (Fig. 2a–d). The dominant foliation in the schist strikes 030°–060° and typically it dips steeply to the SE (Fig. 2a, e). The faults strike subparallel to the Alpine Fault: at Crawford Knob, they crosscut the dominant foliation at a clockwise strike angle of ~23°; and at Chancellor Ridge this angle is ~12°. The faults extend laterally and vertically for up to tens of metres and consistently express both dextral and NW-up senses of slip. Typically, brittle shearing along discrete faults in the quartzofeldspathic schist ceases where the faults intersect quartz veins hosted by that schist. In the veins, shearing is instead viscous. Some of the deformed quartz veins have been smoothly and coherently smeared out to ductile shear strains of up to 15 across shear zones – localized inside the quartz veins – that are ~3 cm wide (Fig. 2c, d). Other quartz veins are offset by a mixture of brittle and ductile slip.

Some of the faults are infilled with fibrous quartz + calcite ± chlorite. In these incrementally grown syntectonic veins alignment of the mineral fibres records the slip direction (Fig. 2f). The fault-infilling veins are ~2 mm wide on average, implying a fault dilation of similar magnitude. The delicate morphology of these fault-infilling fibres (Fig. 2f) suggests that the shearing was accommodated by an aseismic stable sliding process that included dissolution-precipitation creep along the sliding surface (e.g., Gratier and Gamond, 1990; Ohlmacher and Aydin, 1997; Wightman, 2005). The aqueous metamorphic fluids from which the fault-infilling veins were precipitated are inferred to have been released from ductilely deforming rocks that lay beneath the brittle-ductile fault array (Wightman, 2005; Wightman and Little, 2007). Progressive fibre growth would be most likely if the shearing was slow and not abrupt as during an earthquake (e.g., Gratier and Gamond, 1990). Also, the remarkable lack of any brittle fracturing or fragmentation of strongly and smoothly sheared older quartz veins implies that strain rates were low enough to prevent brittle failure. Further, the complete absence of cataclastic or seismically-induced fault rocks along the sharply expressed fault planes in the host schist also indicates that deformation of the schist and the quartz veins was probably due to an aseismic stable sliding process (Little et al., 2002a).

As a result of rapid uplift in the hanging wall of the Alpine Fault and high erosion rates, the biotite zone rocks hosting the shears have been exhumed from > 20 km depth during the past ~3 Myr (Little et al., 2002a). Little et al. (2002a), Wightman et al. (2006), and Wightman and Little (2007) suggest a model for the formation and evolution of the brittle-ductile fault array (Fig. 3). They propose that rocks in the hanging wall of the Alpine Fault were first displaced along a sub-horizontal detachment before being tilted eastward and sheared in an oblique, escalator-like fashion upon reaching the base of the Alpine Fault ramp. As the rocks negotiated the step at the foot of this ramp, they were transiently subjected to high shear stresses and strain rates leading to a temporary embrittlement into the lower crust. This caused the fault array to form in lower crustal rocks that had previously been experiencing only ductile deformation. Alternatively (and perhaps equivalently), this transient embrittlement might be related to movement of overlying brittle faults in the upper crust, associated with straining of the upper crust as it negotiated the Alpine Fault ramp.

Crystallographic preferred orientation (CPO) measurements on sheared quartz veins by Wightman (2005), Wightman et al. (2006), and Hill (2005) has revealed that despite finite ductile shear strains of 5–10, the CPO in them are everywhere very weak to random. Wightman et al. (2006) suggest that a combination of sufficiently reduced grain-sizes through dynamic recrystallisation and rapidly waning stresses towards the end of the shearing process could have allowed for a late increment of diffusion creep-accommodated grain boundary sliding which may have weakened or randomised a pre-existing CPO in the veins (cf. Appendix B).

Due to an elevated thermal gradient in the Alpine Fault hanging wall, the rocks cooled slowly during their rapid exhumation (e.g., Batt and Braun, 1999) and were statically recrystallized. Today, the grain-boundaries in the deformed quartz veins are polygonal (mostly straight grain boundaries and 120° triple junctions; Fig. 4), and the mean grain diameter is 126 ± 16 μm in the sheared part of the vein and 171 ± 14 μm in the unsheared part (2D-grain sizes from Hill, 2005). This microstructure reflects static recrystallisation of the veins subsequent to their ductile shearing (Wightman et al., 2006). We infer that after the rocks were transported away from this ramp corner they did not undergoing any further shearing (Fig. 3, “inactive faults”).

3. Summary of geological and physical constraints on vein deformation

Table 1 summarises important constraints derived from field studies regarding conditions at which vein deformation took place. Further details, and the references on which these estimates are based, are given in Appendix A.

4. Field data – fault-shear zone scaling relationships

We examined several geometric scaling relationships relating to the sheared quartz veins. These were compiled from outcrop exposures of forty-nine wholly ductilely sheared and twenty-three part-brittlely, part-ductilely sheared quartz veins at Chancellor Ridge and Crawford Knob. Fig. 5a illustrates measurements that were recorded on detailed maps of the outcrops after projection of the vein and fault traces into the movement plane using the method of Grigull and Little (2008). For each exposure, we

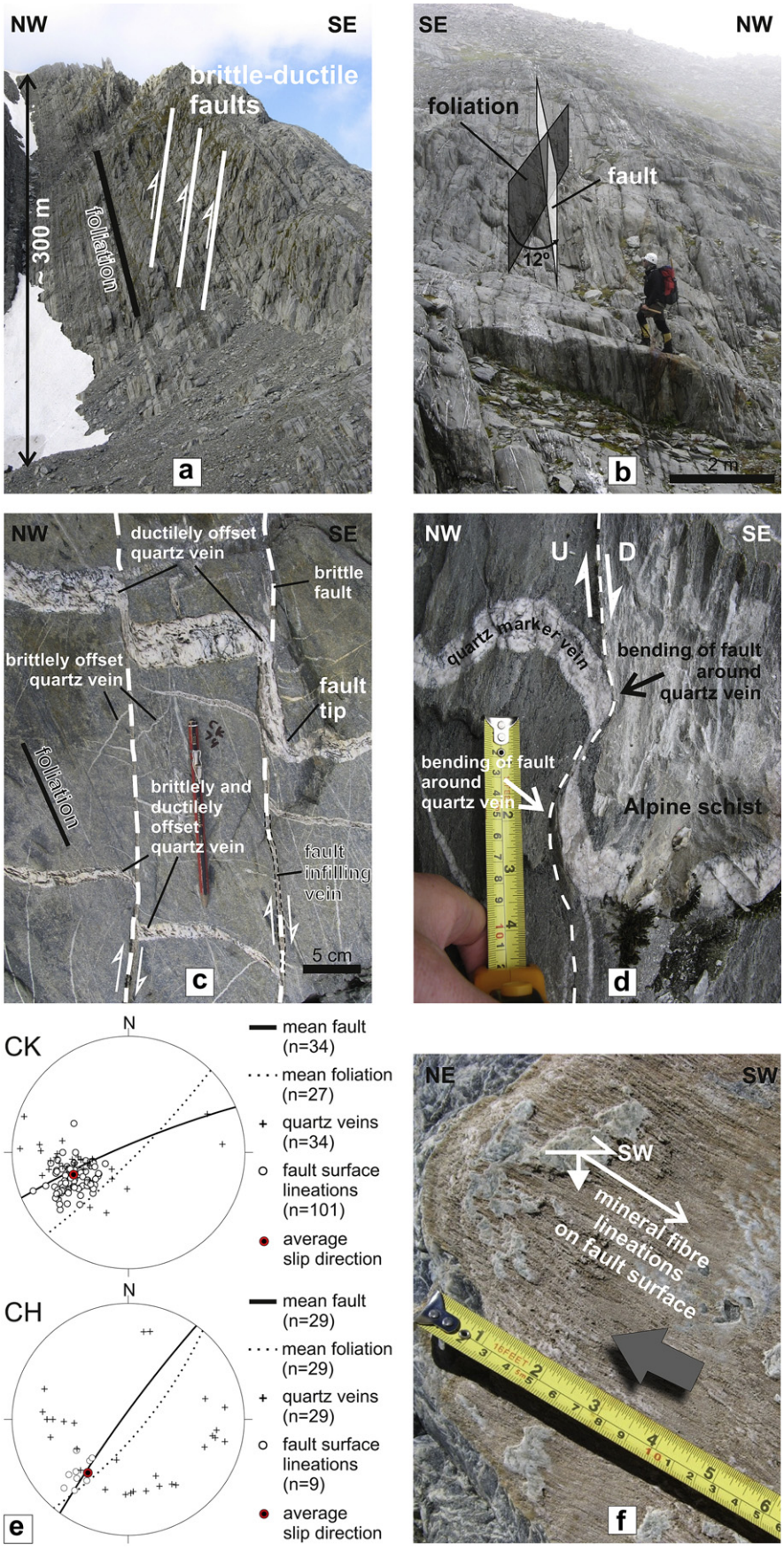
NW
SE
brittle-ductile faults
~ 300 m
foliation
a
SE
NW
foliation
fault
12°
b
2 m
NW
ductilely offset quartz vein
SE
brittle fault
brittlely offset quartz vein
fault tip
foliation
brittlely and ductilely offset quartz vein
fault infilling vein
5 cm
c
NW
U
D
SE
quartz marker vein
bending of fault around quartz vein
bending of fault around quartz vein
Alpine schist
d
CK
N
mean fault (n=34)
mean foliation (n=27)
quartz veins (n=34)
fault surface lineations (n=101)
average slip direction
CH
N
mean fault (n=29)
mean foliation (n=29)
quartz veins (n=29)
fault surface lineations (n=9)
average slip direction
e
NE
SW
SW
mineral fibre lineations on fault surface
f

measured the following parameters: total slip (y_{tot}), brittle slip (b), ductile slip ($d = d_1 + d_2$), original vein thickness (th_{orig}), minimum (strongly deformed) vein thickness (th_{min}), and the fault-normal width of the ductilely sheared part of the vein (dsw). We then used these diagnostic scaling relationships as a filter to distinguish between successful and unsuccessful modelling runs (Section 5).

Although the scatter is large, there is a general increase in the ductile shear zone width (dsw) with increasing undeformed vein thickness (th_{orig}) (Fig. 5b). In other words, the thicker the original vein, the wider the ductile shear zone that later developed inside that quartz vein. The values for the ductilely sheared width range between 1 cm and 4 cm with an average of *c*. 2 cm.

One way to describe the "ductility" (D) of a quartz vein is to specify the ratio between ductile component of slip to total slip ($D = d/y_{tot}$), such that, if $D = 1.0$ the vein has been deformed in a fully ductile manner, and if $D = 0.0$ vein displacement was fully brittle. The plot of ductile/total slip (D) versus original vein thickness th_{orig} shows that most veins with an original thickness greater than ~2 cm are 100% ductilely deformed ($D = 1.0$), whereas veins with thicknesses of less than ~2 cm may show brittle offset as well (Fig. 5c). For $th_{orig} < 2$ cm, no clearly recognisable increase in D with th_{orig} occurs, but an apparently robust observation is that for all but one of the (<2 cm thick) deformed quartz veins which have experienced some amount of brittle slip, the ratio of ductile/total slip is $D \leq 0.5$.

Only veins that have been displaced at least ~3 cm have any brittle slip component ($D \leq 1$), whereas those displaced by < 3 cm are typically only ductilely deformed ($D = 1$) (Fig. 5d). For slips greater than 3 cm, there is no obvious scaling relationship between the ductility of a deformed quartz vein (D) and the finite slip.

The larger the ductile offset of a vein (d), the greater the width of ductile shearing in that vein (dsw) (Fig. 5e). We note that for $d < 3$ cm (especially) this relationship is non-linear. Non-linear retrogression of the data indicates that the scaling relationship between dsw and d seems to follow a power law (Fig. 5e).

We define the vein attenuation factor $th_{att} = th_{min}/th_{orig}$ to be the ratio of the minimum thickness of the most deformed part of a sheared vein (th_{min}) to the inferred original thickness of that vein (th_{orig}) as preserved in the external part of a vein away from the shear zone. The greater the ductile offset (d) is, the more attenuated the vein (Fig. 5f). At a ductile displacement of just 2 cm, most of the wholly ductilely deformed quartz veins have already been thinned to at least 40% of their original thickness. At offsets greater than 2 cm th_{att} decreases with a relatively shallow gradient. This leads us to infer that these two scaling parameters are related by a power law with a negative power law exponent. Non-linear regression suggests a power law (Fig. 5f).

5. Numerical experiments

Section 4 shows that there are systematic scaling relationships between several geometric parameters related to the brittle to ductile shearing of the quartz veins. These are inferred to reflect aspects of the rheology during deformation. In order to refine our understanding of the rheological properties of these natural quartz veins, we have modelled several vein deformation scenarios in an attempt to replicate the observed patterns, constrained by deformation conditions summarised in Table 1.

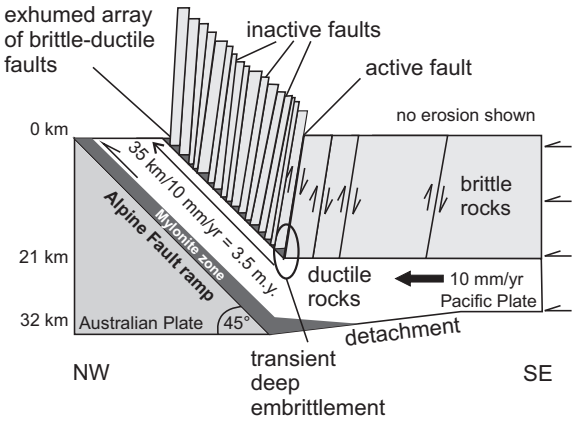

Fig. 3. Escalator model after Little et al. (2002a) and Little (2004). Pacific Plate rocks are delaminated along a detachment and undergo transiently high shear stresses and embrittlement when they pass the foot of the Alpine Fault ramp. After passing this critical point, hanging wall deformation stops and the rocks get transported to the surface (inactive faults).

5.1. Experimental framework – rheological end-members

The field observations indicate that narrow brittle faults offset the quartzofeldspathic host schist, but that these faults commonly do not fully penetrate pre-existing quartz veins embedded within the schist that the faults encounter along their length. Instead, the quartz veins were mostly subject to ductile shearing. However, as detailed in Section 4, not all the quartz veins underwent purely ductile deformation, as some also experienced a component of brittle slip. Moreover, we observed some ductile deformation of the quartzofeldspathic wall rock schist in the deeper structural levels of the fault array. This might be attributed to higher deformation temperatures in the deeper parts of the otherwise brittle fault array leading to lower flow strength of its wall rocks (Wightman, 2005). In the rest of the array, macroscopic ductile deformation of the host schist is localised in step-over zones between two non-coplanar faults (Fig. 6). We infer that the strain rates across these step-over zones were low enough to enable ductile flow in the schist host instead of brittle faulting. The ductile deformation of the schist in those step-overs is usually expressed as a rotation of the dominant foliation that is consistent with dextral shearing along the two adjacent faults (Fig. 6).

To accord with the field observations, our numerical models for the quartz veins and the quartzofeldspathic host rocks that enclose those veins include both a "frictional-plastic" (i.e., brittle) material behaviour and a "viscous" (i.e., ductile) one. Fig. 7 overviews possible combinations of brittle and viscous material behaviours in the schist and the quartz. Cases A–E (black outlines in Fig. 7) are the most common in the field, with fully brittle or brittle-viscous

Fig. 2. Rocks and structures in the brittle-ductile fault array. Note the consistent dextral, NW-up sense of movement of the faults in all photographs. a) Cliff at Crawford Knob, showing near-vertical brittle-ductile faults with respect to the dominant foliation. b) Glaciated outcrops near Chancellor Ridge. The superposed planes indicate the angle between the main foliation and the planar brittle-ductile faults which is everywhere observed to be ~12°. c) Outcrop photograph, Crawford Knob. Here, brittle faults offset the host quartzofeldspathic Alpine Schist as well as some of the thinnest (<1 cm) quartz veins embedded in that schist. Where the tips of the faults truncate thicker quartz veins, they deform them brittlely-to-ductilely or entirely ductilely. The dashed line marks a fault-infilling vein. d) Single quartz vein from Crawford Knob being displaced fully ductilely where a brittle fault in the host schist intersects the vein. Note how the fault bends around the outside margin of the deformed quartz vein and the extreme vein attenuation in the shear zone centre, which is typical for the ductilely shearing veins. e) Mean attitudes of brittle faults, mean foliation, poles to deformed quartz veins, fault surface lineations, and average slip direction plotted on lower hemisphere, equal area stereographic projection. CK = Crawford Knob, CH = Chancellor Ridge. f) Photograph of quartz + calcite + chlorite vein infilling brittle faults. Incrementally grown fibre lineations indicate the direction of slip. The grey arrow points in the direction in which the (now eroded) hanging wall moved.

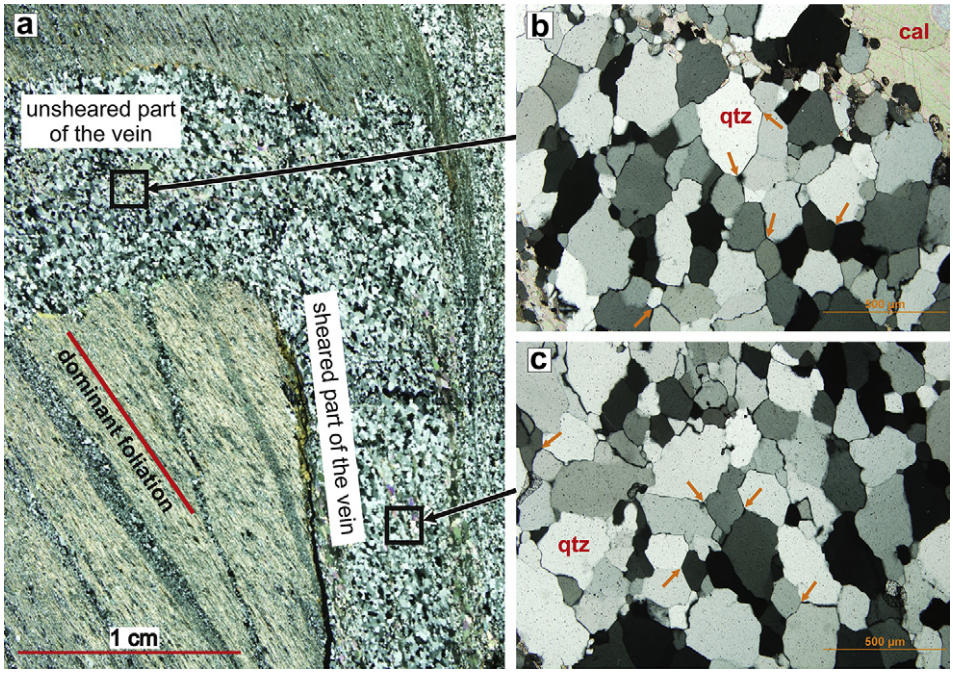

Fig. 4. Photomicrographs of a ductilely sheared quartz vein from Crawford Knob under crossed polars. a) Stitched photomicrograph of deformed vein. Note the smooth, fracture-free bend in the quartz vein where the shear zone transects it. The dominant foliation is clearly expressed by biotite alignment in the wall rock schist. b) Statically recrystallised, foam-like microstructure in unsheared part of the vein, external to the ductile shear zone. c) Statically recrystallised microstructure in sheared part of the vein, internal to the ductile shear zone. Note how similar the polygonised grain shapes and the microstructure are in both the sheared and the unsheared part of the quartz vein. Orange arrows point to 120° triple junctions, showing the polygonised grain shapes (For interpretation of the references to colour in this figure legend, the reader is referred to the web version of this article.).

behaviour of the host schist; and fully viscous, brittle-viscous, or fully brittle behaviour of the quartz veins embedded in that schist. Even at locations in the field where the quartzofeldspathic schist exhibits ductile deformation, we always infer a precursory brittle fracture to have affected that everywhere faulted host schist. For this reason we did not attempt to model the rheological end–member combinations depicted in cases F–I (grey outlines in Fig. 7) as these would produce only viscous structures in the schist.

Table 1
Physical constraints on vein deformation. Details on derivation of constraints can be found in Appendix A.

Constraint	Best estimate	Notes	References
Time available for exhumation of fault array from 25-27 km depth to surface	3.5–3.8 Myr	Assuming Alpine Fault fault dips 45° and its dip-slip rate is 10 mm/yr. Fault array forms at 5–7 km above 32 km-deep basal detachment	Norris and Cooper, 1995, 2001; Stern et al., 2001; Wightman, 2005
Time available for vein deformation and subsequent annealing during exhumation from 25-27 km to 10 km depth	≤1.5 Myr	Assuming that quartz crystal-plasticity ceases at ~300 °C, and assuming 300° C-isotherm at ~10 km depth; also assuming Alpine Fault dips 45° and its dip-slip rate is 10 mm/yr	Shi et al., 1996; Batt and Braun, 1999; Stöckhert et al., 1999; Leitner et al., 2001
Temperature (T) during vein deformation and precipitation of fault-infilling veins	350–500 °C	Ti-in-quartz thermometry in deformed veins and quartz-calcite oxygen isotope thermometry in fault-infilling veins	Wightman, 2005; Wark and Watson, 2006; Grigull, 2011
Depth (z) of faulting and vein deformation	≥21 km	$^{40}Ar/^{39}Ar$ muscovite cooling ages in host rock are 3.4–4.5 Ma, assuming closing temperature was ~400 °C and closure subsequent to deformation; assuming an Alpine Fault dip of 45° and a dip-slip rate of 10 mm/yr yields depth estimate	Lister and Baldwin, 1996; Wightman, 2005 ($^{40}Ar/^{39}Ar$ data from S. Baldwin); Grigull, 2011
Lithostatic Pressure (P_{lith})	≥560 MPa	$P_{lith} = \rho gz$; and $z = 21$ km	–
Differential Stress (σ_d)	≥100 MPa	Mohr-Coulomb-Griffith analysis of brittle fracture for intact rock (independent of depth or fluid pressure)	Wightman, 2005; Grigull, 2011
Fluid pressure (P_f) at time of fault initiation	500–530 MPa	near-lithostatic P_f required to cause brittle failure at $z = 21$ km and at $\sigma_d = 100$ MPa	Stern et al., 2001, 2007; Wightman, 2005; Grigull, 2011
Fluid pressure (P_f) at time of fault initiation	310 ± 90 MPa	P_f during entrapment of fluid inclusions in fault-infilling veins determined from fluid inclusion isochores combined with oxygen thermometry of fault-infilling veins	Wightman, 2005; Grigull, 2011
Max. fault slip rates ($\dot{y}_{max}$) $\dot{y}_{max} = y_{tot}/dt_{min}$	~2 mm/yr	Assuming sequential activation/deactivation of shears and only one shear active at a time; mean shear spacing ($S = 37$ cm) divided by plate convergence rate (10 mm/yr) implies a per-shear duration of shearing of $dt_{min} \approx 37$ years; average total slip on one fault is $y_{tot} = 70$ mm	De Mets et al., 1990, 1994; Norris and Cooper, 2001; Wightman and Little, 2007
min. fault slip rate ($\dot{y}_{min}$) $\dot{y}_{min} = y_{tot}/dt_{max}$	~3.6×10^{-4} mm/yr	assume all faults active simultaneously; width of entire shear array ($S = 2$ km) divided by plate convergence rate (10 mm/yr) implies duration of shearing $dt_{max} \approx 200$ kyr; average total slip on one fault is $y_{tot} = 70$ mm	Wightman and Little, 2007

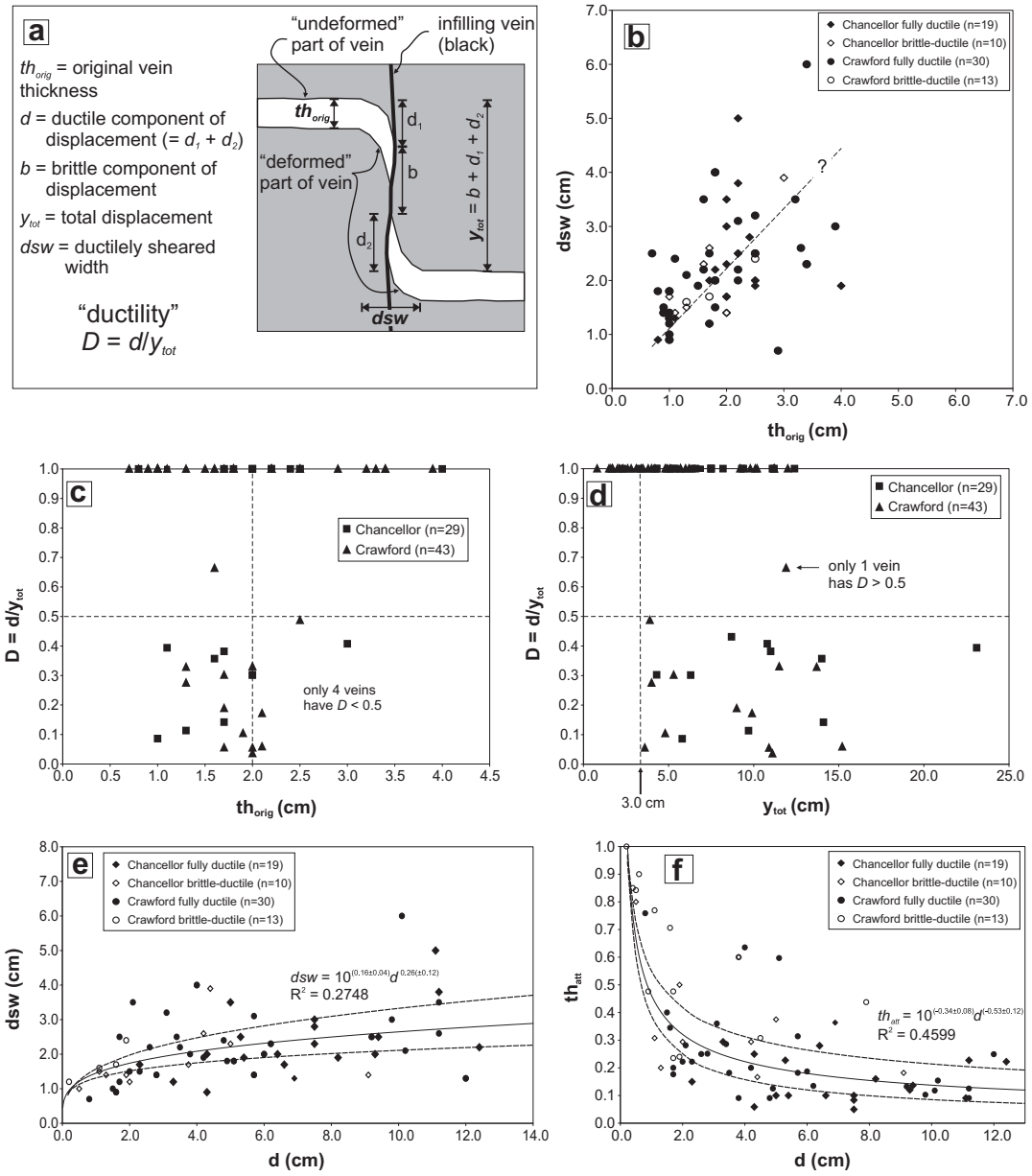

Fig. 5. Field data-derived plots of scaling relationships measured in the quartz veins. All data have been separated by location and 'ductility'. Measurement uncertainty is ±0.2 cm. Where plausible, we put trendlines through the field data. a) Schematic overview of measurements that were taken from the vein-fault sets after having been projected into the movement plane of the brittle faults. b) Ductilely sheared width (dsw) vs. original vein thickness (th_{orig}). c) Ratio ductile/total slip (D) vs. original vein thickness (th_{orig}). d) Ratio ductile/total slip (D) vs. total slip (y_{tot}). e) Ductilely sheared width (dsw) vs. ductile component of slip (d). f) Vein attenuation factor (th_{att}) vs. ductile component of slip (d). The dashed lines in e) and f) correspond to the errors calculated for the trendlines.

5.2. Description of numerical technique

We use a version of the two-dimensional Lagrangian-Eulerian finite element code SULEC (developed by Susan Ellis and Susanne Buiter) that has been specifically adapted for this study to investigate the effect of rheology, geometry, and deformation history on vein shape and flow mechanism. We have benchmarked SULEC against the commercial Lagrangian finite element code "Abaqus" (Abaqus/Standard version 6.7; Simulia, Providence, RI) and attain similar results, for small deformation (Grigull, 2011). SULEC solves the Stokes equation for slow creeping flows (e.g., Fullsack, 1995; Moresi et al., 2003) on an Eulerian grid which is held fixed here. Material properties and strain are stored on tracers which are advected through this stationary grid. This approach allows large finite strains to accumulate without affecting the quality of the computational mesh (cf. Abaqus/Standard). Pressure is here solved via a penalty approach. The rheology is either viscous or brittle (frictional-plastic) depending on which mechanism attains the lowest effective stress (e.g., Fullsack, 1995).

5.3. Model setup

We set up four model series in order to examine different aspects of the rheology in the brittle-ductile shear array, especially the interplay between viscous and brittle deformation ahead of the fault tip in the deformed quartz veins. All models include a quartz vein and a fault propagating from the upper and lower boundaries towards the quartz vein (Fig. 8).

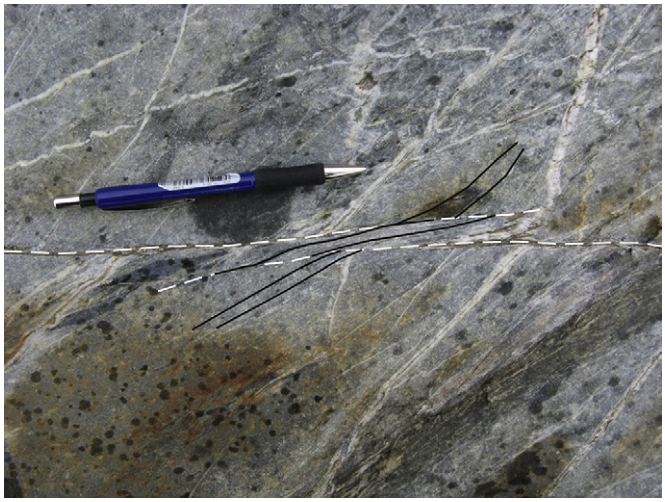

Fig. 6. Example of the ductile deformation of quartzofeldspathic schist localised to the step-over zones between two non-coplanar faults. The two fault terminations (white stippled lines) are overlapping and the rotation of the foliation (black lines) is consistent with dextral shearing along those faults. The overlapping zone is c. 2 cm wide and c. 14 cm long.

5.3.1. Initial geometry and boundary conditions

The initial model dimensions are 0.1 m × 0.1 m (Fig. 8). The structured mesh resolution is 100 × 100 square elements so that element resolution is 1 × 1 mm. Each element originally contains four tracers amounting to a total of 40,000 tracers in the entire model, with an automated tracer injection scheme to maintain sufficient tracer density in each element. An initially horizontal quartz vein is embedded in the middle of the model. The quartz vein can be included into the model with different original thicknesses (th_{orig}).

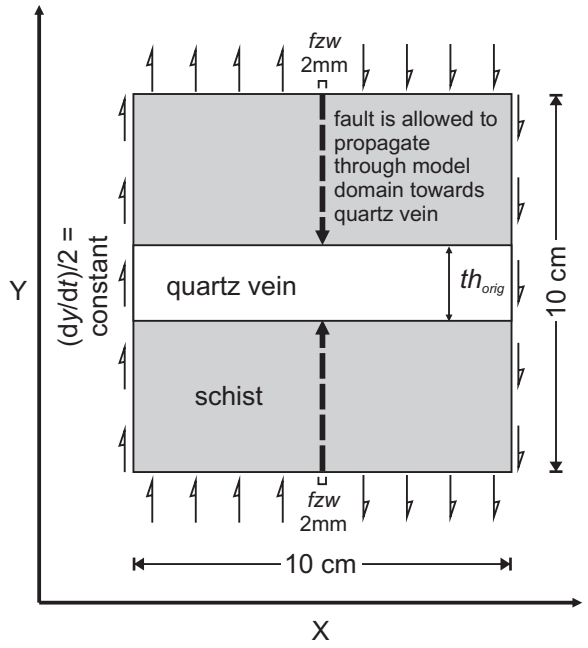

Fig. 8. Initial model setup for numerical modelling. $(dy/dt)/2$ is half of the externally imposed total slip rate (dy/dt) on the fault. *fzw* is the prescribed fault zone width (2 mm, equalling the mean dilative width of the fault-infilling quartz-calcite veins). Note that there is no pre-existing fault but that we model the propagation of a brittle fault through the schist into the quartz vein.

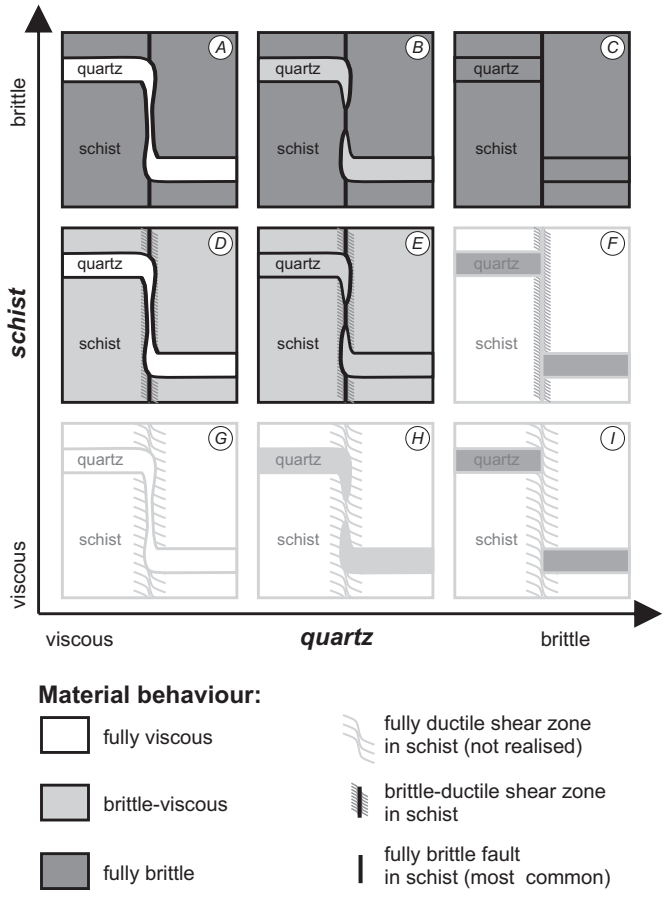

Fig. 7. Overview of possible combinations of the two end-members brittle (dark grey) and viscous (white) deformation in the quartz and the schist. Brittle-viscous deformation is marked in light grey. Cases A-E are the most common cases in our area. Cases F–I (no brittle component in schist) were not observed in the field.

We apply constant velocity boundary conditions (dy/dt = 0.5 mm yr^{-1}, Fig. 8) around the model domain in order to simulate fault slip in the schist external to the embedded quartz vein and the in-plane propagation path of that fault towards the vein (see Appendix A4 for the field equivalent of these velocity boundary conditions). The width of the external fault zone at the top and bottom of the model is set to 2 mm (*fzw*, Fig. 8). This equates to the average dilative thickness of the fault-infilling veins measured in the field (~1.9 mm).

Since the veins accumulate a large finite ductile shear strain at sub-dynamic strain rates (cf. Section 2.2), we assume that the faults did not form first as dynamic cracks, but underwent a slow propagation. The numerical models are a two-dimensional representation of three-dimensional fault geometry and it is probable that the brittle faults propagated partly out of plane around the veins. Therefore, we chose to model a fault propagating into the modelled domain rather than setting the fault as an initial condition and imposing its geometry. This accords with field observations showing that the brittle faults interact with the quartz veins and are usually deflected around them (Fig. 2d).

5.3.2. Material parameters used in model series 1–4

5.3.2.1. Brittle yield strength. As justified in Appendix A3, we chose an initial brittle yield stress for the intact schist of τ_f^s = 50 MPa (corresponding to a differential stress of σ_d^s = 100 MPa). Plastic strain softening is active in the schist in order to achieve strain localisation in the fault zone (Fig. 8). The schist is softened to τ_f^s = 15 MPa after accumulation of ~10% plastic strain (measured as the second invariant of the strain tensor) resulting in a narrow fault

zone (Appendix C). This is in agreement with long, discrete, well-formed faults that are seen in the field, some of which have offsets of only a few millimetres.

In model series 2 and 3 we also incorporated a brittle yield stress in the quartz. The quartz brittle yield strength was also set at $\tau_f^q = 50$ MPa, the same as for the quartzofeldspathic schist. We assumed that the quartz did not undergo brittle strain-softening, because the shear zones in the quartz veins appear less localised than the narrow, discrete faults in the schist host rock (e.g., Fig. 2d).

5.3.2.2. Viscous rheology. Assuming that the main active deformation mechanism was grain size-independent dislocation creep in the quartz vein (Appendix B; Wightman et al., 2006), we can exclude the grain-size term in Eq. (1) and simplify it to:

$$\dot{\varepsilon}_S = A_M \cdot \tau_v^n \tag{2}$$

where $\dot{\varepsilon}_S$ is the shear strain rate as defined in Appendix D, and τ_v is the (flow) stress in shear. Factor A_M is a material constant that includes the experimentally derived pre-exponential factor A_E, water fugacity f_{H_2O}, the exponential term $\exp(-Q/RT)$, and a geometry factor G necessary for the conversion from triaxial experiments to plane strain (Ranalli, 1987):

$$A_M = G \cdot f_{H_2O} \cdot \exp\left(-Q/RT\right) \cdot A_E \tag{3}$$

Since water fugacity is included in Eq. (3), A_M is in the units of [MPa^{-n} s^{-1}].

In all experiments we chose a constant temperature of 450 °C (cf. Section 3). We used an activation enthalpy of $Q = 135$ kJ/mol (Paterson and Luan, 1990; Hirth et al., 2001). For a lithostatic pressure of 560 MPa at ~21 km depth and a temperature of 450 °C, we estimated a water fugacity of $f_{H_2O} = 200$ MPa under fully water-saturated, near-lithostatic fluid pressure conditions (using published fugacity coefficients, cf. Appendix B). In order to derive varying strength ratios in the numerical models, we changed A_M-values in the quartz vein in model series 1 and 2 as well as in the schist in model series 4. In model series 1 and 3, we also varied the stress exponent n between 1 and 4, adjusting A_M-values appropriately.

5.3.2.3. Contrast between viscous strength of quartz and brittle strength of schist. We define the quartz-to-schist viscous-to-brittle strength contrast between the two materials, quartz (mostly viscous) and schist (mostly brittle), to be equivalent to the ratio

$$R^{qs} = \tau_v^q / \tau_f^s \tag{4}$$

where τ_v^q is the viscous (ductile) flow strength of the quartz, and τ_f^s is the frictional-plastic (brittle) yield strength of the unsoftened schist. For example, using a water fugacity of 200 MPa, and Hirth et al.'s original A_E-value ($10^{-11.2}$ MPa^{-n-m} s^{-1}), we calculated a material constant of $A_M = 10^{-17.76}$ MPa^{-n} s^{-1} in Eq. (3). Using $A_M = 10^{-17.76}$ MPa^{-n} s^{-1} in Eq. (2), and a shear strain rate of 3.95×10^{-9} s^{-1} (corresponding to a total differential velocity of $dy/dt = 0.5$ mm/yr) over a fault zone width of 2 mm, we calculate a flow stress near the fault tip in the quartz vein of $\tau_v^q = 219$ MPa. Using $\tau_v^q = 219$ MPa and $\tau_f^s = 50$ MPa with Eq. (4) would give a strength contrast of $R^{qs} = 4.38$. Note that the calculated flow stress is only a theoretical value, since it is based on the assumption that the 2 mm wide shear zone is maintained throughout the quartz vein once the "brittle" fault encounters the model vein. In reality, deformation spreads out in the quartz, and strain rates and flow stresses decrease there.

5.4. Results – model series 1: influence of the viscous-to-brittle (quartz-to-schist) strength contrast (R^{qs}) and of the flow law stress exponent (n) on the propagation behaviour of the brittle fault

In this section, we investigate the influence of R^{qs} for a wholly ductile quartz vein and purely brittle schist (Fig. 7, case A) on the propagation behaviour of the fault through the schist and into the quartz vein. All of the following models include a 2 cm thick horizontal quartz vein at right angles to the fault.

In order to qualitatively test in which way the propagation and/or bifurcation of the brittle fault in the schist host rock might depend on R^{qs} and the stress exponent of the quartz vein (n_q), we set up models with different R^{qs} -values (0.01, 1.2, 5.0, 13.2). For these (theoretical) ratios τ_v^q was calculated via Eq. (2) for different A_M-values, a nominal initial strain rate of 3.95×10^{-9} s^{-1} at the fault-quartz vein intersection, and two different stress exponents ($n_q = 1$ and $n_q = 4$). We prescribed that the brittle yield stress in the quartz is never reached by setting the brittle yield stress for the quartz to 10 GPa (i.e., $\tau_v^q << \tau_f^q$), whereas to ensure purely brittle behaviour in the schist, the flow strength in the schist was chosen to be significantly higher than its brittle strength (i.e., $\tau_v^s >> \tau_f^s$). Table 2 summarises the material parameters that were used in the models.

5.4.1. Results

Fig. 9 shows contour plots of strain rates after 5, 25, and 100 years of deformation. Models with a linear viscosity in the quartz vein ($n_q = 1$) are denoted with "L" whereas models with a power law quartz rheology ($n_q = 4$) are denoted with "P". R^{qs} is labelled above the model-plots.

During early stages of the deformation, there are large differences in fault localisation between the linear and the power law model types (Fig. 9, 0.25 cm displacement after 5 yrs). In all the models with a linear quartz vein rheology (L-models), the fault in the model schist does not localise but bifurcates at a distance of roughly $\sim th_{orig}$ (where th_{orig} is vein thickness) from the quartz veins for all calculated strength contrasts. The two branches of the split-up faults are connected through sub-horizontal cross-shears, creating "Eiffel-Tower"-patterns in the strain rate contours. The models with the power law quartz rheology (P-models) show fault bifurcation for R^{qs} -values of 0.01, 5.0, and 13.2. However, model P2 with a viscous-to-brittle strength contrast (quartz/schist) of 1.2 shows a well localised fault even at the early stages of deformation (Fig. 9; 'no bifurcation').

The Eiffel-Tower-patterns in L1 to L3 and in model P1 develop because in those models, the quartz vein is so weak ($\tau_v^q << \tau_f^s$), that the vein–schist interface acts like a free boundary in the quartz allowing strain accommodation through the rotation of small schist blocks between the fault branches. The vortical motion of those "blocks" is impeded by the stiffness of the schist, leading to the

Table 2
Material parameters used in section 5.4. R^{qs} is ductile-to-brittle strength contrast between viscous quartz and brittle schist, Eq. (4). Numbers in table are corresponding values of $\log_{10}(A_M)$. L-models assume a linear viscous rheology with a flow law stress exponent $n_q = 1.0$ and P-models power law creep in the quartz vein with $n_q = 4.0$.

viscous-to-brittle (quartz-schist) strength ratio R^{qs}	0.01	1.2	5.0	13.2
$\log_{10}(A_M)$ [MPa^{-n} s^{-1}] for L-models ($n_q = 1.0$)	−8.1	−10.2	−10.8	−11.0
$\log_{10}(A_M)$ [MPa^{-n} s^{-1}] for P-models ($n_q = 4.0$)	−7.2	−15.5	−18.0	−19.7

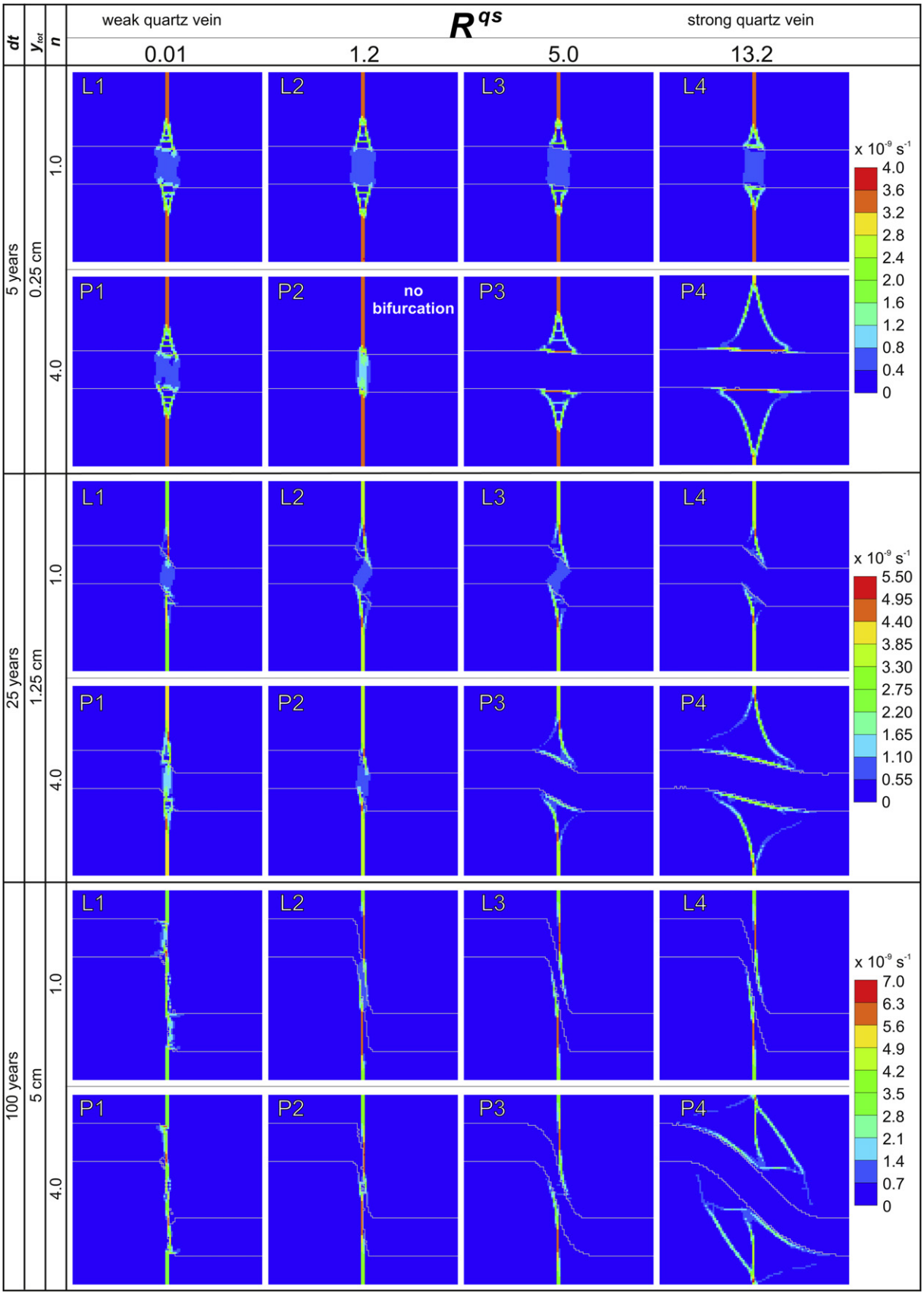

Fig. 9. Results of model series 1 – Influence of a viscous layer (quartz vein) on the propagation behaviour of an external brittle fault. Model plots are strain rate contours at 0.25, 1.25, and 5 cm total vein displacement. R^{qs} is the viscous-to-frictional strength ratio between the ductilely deformed quartz and the brittlely yielding schist. Effective viscosity is increasing towards the right. L-models use linear viscosity, P-models use power law quartz rheology. Note the 'Eiffel-Tower'-patterns (e.g., L1, P1) in the models with the weak quartz layers and the tent-like patterns in the models with a strong quartz (e.g., P4). P2 is the only model that has a fully and well localised fault from the beginning of deformation ("no bifurcation"). Note also, that the fault in none of the L-models ever localises in the initial stages of deformation.

formation of strain-softened sub-horizontal cross-shears. This phenomenon is discussed in more detail in Section 6.1.

In models P3 and P4, slip occurs at the quartz vein–schist interface in the schist. In P3, the fault bifurcates and rotational cross-shears form in the schist. In P3, the viscous yield in the quartz vein is much higher ($\tau_v^q = 250$ MPa) than the brittle strength of the schist in the unsoftened ($\tau_f^s = 50$ MPa; and $R^{qs} = 5$) or the softened state ($\tau_f^s = 15$ MPa). This means that almost the entire deformation needs to be accommodated by the schist. The stiff quartz vein impedes the rotation of the schist blocks, leading to the cross-shears in the strain-softening schist. In contrast, model P4 ($R^{qs} = 13.2$) shows a tent-like pattern without the formation of cross-shears. Here, the quartz vein is so strong ($\tau_v^q >> \tau_f^s$) that it acts almost like a rigid block, forcing the deformation to spread out in the quartz and enhancing fault bifurcation in the schist. The tent-like appearance of the fault in P4 is due to the top and bottom boundary conditions that force the model to initiate faulting at the imposed 2 mm wide zone (Fig. 8, model setup). If the top and bottom boundaries of model P4 were instead free and the location of fault initiation was not predefined, one would expect two separate (sub-parallel) shears to form at these boundaries.

At higher displacements, all the models with a linear quartz rheology (L-models) and all the power law models (P-models) except P4 start to abandon one branch of the initially bifurcating faults. This is partly due to the external asymmetric velocity boundary conditions, but it is mostly an effect of progressive vein rotation and attenuation, since the shears prefer to take the "path of least resistance" in order to minimise the energy dissipation in the system (see Section 6.1). In models L1 and P1, the path of least resistance is through the quartz vein, since it has a low effective viscosity; i.e., a lower strength than the schist. This results in the shear bending *into* the quartz vein (Fig. 9, L1 and P1 at 5 cm displacement). Conversely, in models L2, L3, L4, and P2, P3, where effective quartz viscosities are higher, the path of least resistance is along the quartz-schist boundary, and the shear takes the shortest path through the quartz vein, resulting in the shear bending *around* the quartz vein. In the field, we chiefly observe the latter: a shear bending around the quartz vein (e.g., Figs. 2c, d and 9). The fault in model P4 also abandons its left branch, but because of the high strength of the quartz, an additional new branch has formed in between the two older ones at 100 years of deformation.

From the results of modelling series 1, we infer that the brittle-viscous strength ratio between the schist and the quartz veins strongly controls the localisation and propagation of the brittle fault. In the field, we usually observe a well localised fault intersecting a quartz vein without bifurcating at the intersection with the vein. This suggests that R^{qs} was probably close to 1.0 during the shearing of the veins, i.e. that $\tau_v^q \approx \tau_f^s$.

5.5. Results – model series 2: brittle-ductile transition in the quartz veins

In this section we investigate which deformation conditions (A_M-values, initial vein thickness, and total displacement) allow a quartz vein embedded in a brittlely faulted schist to deform with mixed ductile and brittle components where it encounters that fault. The following models represent cases A–C in Fig. 7.

5.5.1. Vein thickness th_{orig} and A_M-values

We first set up models that include a horizontal quartz vein each with a thickness range of 0.5 cm–3.0 cm with 0.5 cm steps in between. The brittle yield strength in the quartz veins for these models was set to $\tau_f^q = 50$ MPa, identical to that of the intact schist, and we used the same entirely brittle schist rheology as in Section 5.4 ($\tau_f^s << \tau_v^s$).

Table 3
Model parameters for testing the brittle-ductile transition in the quartz veins.

A_M (MPa^{-n} s^{-1})	τ_v^q (calculated flow stress)	$R^q = \tau_v^q/\tau_f^q$
6.35×10^{-16}	50 MPa	1.0
3.06×10^{-16}	60 MPa	1.2
1.65×10^{-16}	70 MPa	1.4

Under these boundary conditions, brittle yielding of an intact quartz vein will depend on the ratio of the calculated flow stress to the brittle yield stress in that vein ($R^q = \tau_v^q/\tau_f^q$) and on its thickness. We set up models with different R^q -values by changing the A_M-value for the quartz flow law (Table 3). For all of the following models, a stress exponent of $n = 4.0$ was used.

In Fig. 10 we plot the ratio D against the original vein thicknesses th_{orig} at a total model displacement of 5.0 cm (i.e., after 100 years of deformation). For all three R^q -values, there is a positive but non-linear correlation between th_{orig} and the ratio D with the ductile component of slip increasing with increasing initial vein thickness (Fig. 10). For $R^q = 1.0$ and $R^q = 1.2$ only the 2.5 cm and the 3.0 cm thick veins have deformed entirely ductilely, whereas the veins with thicknesses ≤2.0 cm all yield brittlely as well. For $A_M = 1.65 \times 10^{-16}$ MPa^{-n} sec^{-1} ($R^q = 1.4$) all but the 3.0 cm thick veins are ductilely and brittlely deformed. The reason for the 'bump' (stippled line in Fig. 10) in the curve for $R^q = 1.4$ is due to the veins thinner than 2.5 cm yielding brittlely first, then ductilely (see Section 5.5.2 below).

In summary, the numerical models show that the D-value of a sheared quartz vein not only scales with the original undeformed vein thickness, but also depends strongly on the ratio between viscous and brittle yield strength for quartz in the quartz veins (R^q). The brittle-ductile transition in the quartz veins seems to be very sensitive to R^q. Even small changes (±10 MPa) in the calculated flow strength can apparently control whether a quartz vein yields brittlely or ductilely and how high the resulting brittle component of slip is. When compared to the field data, the models with $R^q = 1.2$ and $R^q = 1.4$ are the best fit.

5.5.2. Total vein displacement y_{tot}

To find out the influence of total displacement on the ratio of ductile to total slip (D), we increased the vertical extent of the models to 0.2 m to attain displacements of up to 10 cm. We verified

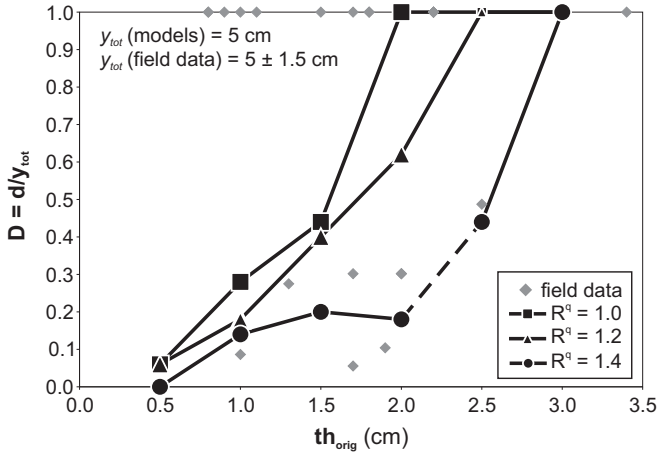

Fig. 10. Results of model series 2 – Plot of "ductility" D against original vein thickness th_{orig} at a total displacement of $y_{tot} = 5$ cm. Only field data with y_{tot} between 3.5 and 6.5 cm are shown. $D = 1.0$ is fully ductile, $D = 0.0$ is fully brittle. The data suggests that D increases with original vein thickness. The kink in the line for $R^q = 1.4$ expresses the modelled relationship that all veins that were originally thinner than 2 cm are predicted to fail brittlely first. Those veins acquire a final D-value of less than 0.2.

that results were similar to thinner models when deformed to 5 cm displacement.

Fig. 11a–c shows the ratio of D versus total displacement y_{tot} for the different vein thicknesses and the three A_M-values that were used in the models. For $A_M = 6.35 \times 10^{-16}$ MPa^{-n} sec^{-1} ($R^q = 1.0$) the 0.5, 1.0, 1.5, and 2.0 cm thick veins show a non-linear inverse relationship between the ratio D and the total displacement y_{tot}, i.e., the higher the displacement, the lower D (Fig. 11a). The model with the thinnest quartz vein ($th_{orig} = 0.5$ cm) produces the curve with the steepest gradient.

Fig. 11b shows the plot of D versus total displacement for $R^q = 1.2$ for different vein thicknesses. It is evident that there are two ways for a quartz vein to accommodate mixed brittle-ductile offsets: i) the two veins with $th_{orig} = 0.5$ and 1.0 cm both fail brittlely at first, and then deform ductilely with increasing slip, since strain rates wane away from the vein centres and deformation can spread out through viscous flow; ii) the quartz veins that were initially thicker than 1.0 cm deform viscously at first and then yield brittlely at a total displacement greater than 2.5 cm. This is due to ductile vein thinning so that the two stress tips at the fault tips are able to meet and join.

For $R^q = 1.4$, all veins but the 3 cm thick vein yield brittlely first, after which they start to deform viscously (Fig. 11c). The 0.5 cm thick vein stays fully brittle. Interestingly, the models show that if the quartz veins fail brittlely before reaching their flow yield stress, final D-values of all those veins are <0.5 at $y_{tot} = 5$ cm. The veins achieve a temporary peak in D before this ratio starts to decrease again as slip on the fault accumulates.

5.6. Results – model series 3: influence of stress exponent n_q on deformed quartz vein shape

In model series 3 we investigate the sensitivity of the final shape of the sheared quartz veins to the stress exponent n_q in Eq. (2) in the quartz veins. We used 0.1 × 0.1 m models with a 2 cm thick horizontal quartz vein. The brittle yield stress was 50 MPa in both the

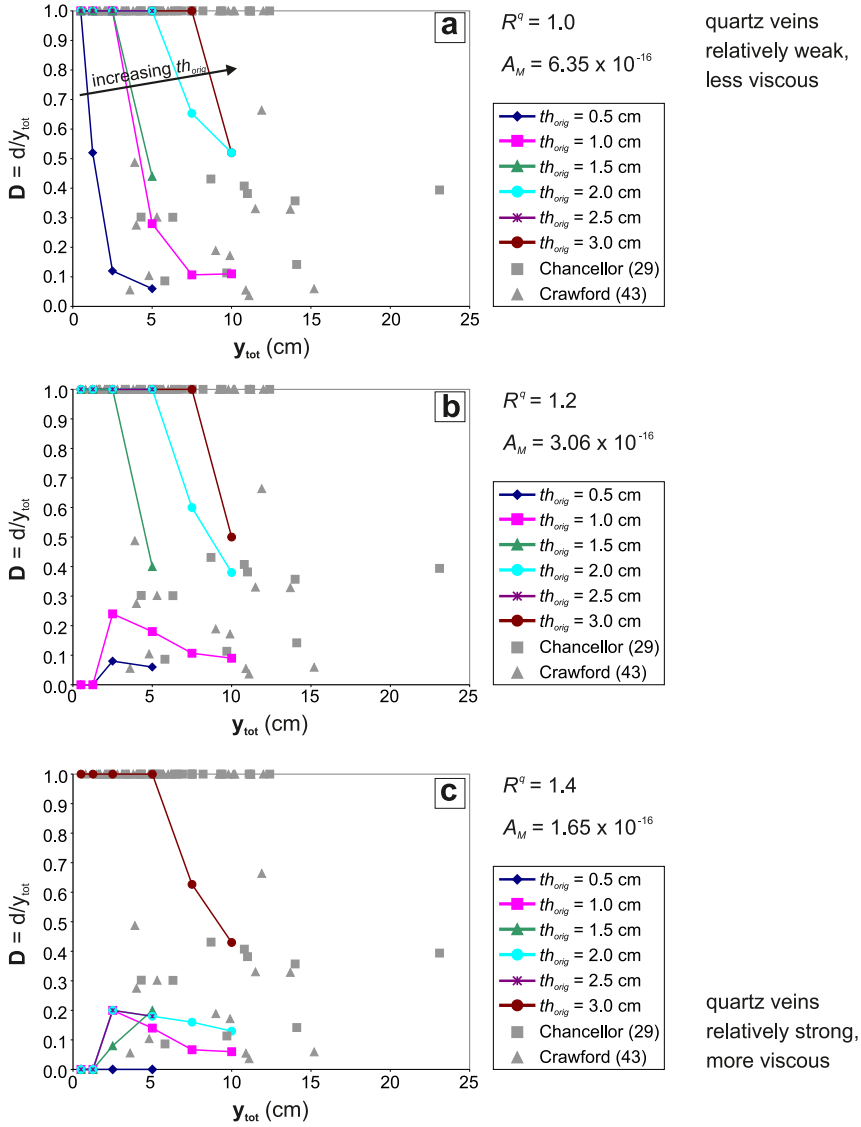

Fig. 11. Results of model series 2 – plot of ductility D against total displacement for different R^q values. Each coloured line represents a different original vein thickness th_{orig}. These graphs show that there is a relationship between total displacement (y_{tot}) and vein ductility (D): the higher y_{tot}, the lower D. It is also evident from these graphs that two different failure sequences can occur: i) ductile yield first, then brittle as for all veins in (a), ii) brittle first, then ductile as for example in (c). See text for detail.

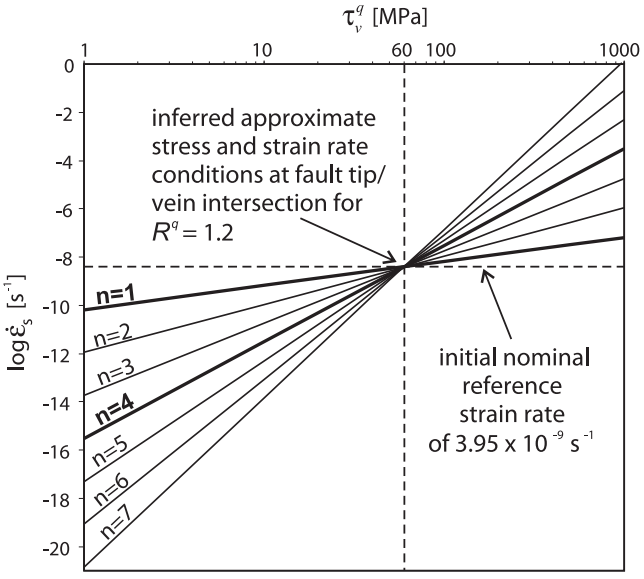

Fig. 12. Log–log plot of strain rate versus viscous flow stress to determine the pre-exponential factor A_M. The stress exponent n determines where the lines cut the strain rate axis. This interception point gives A_M. The flow law of Hirth et al. (2001) was modified to accord with our plane strain numerical experiments and to include a calculated water fugacity of 200 MPa at the field site during deformation. All lines intersect at a flow shear stress of 60 MPa for a viscous-brittle strength contrast in the quartz of $R^q = 1.2$ (see main text for details) and an initial strain rate of 3.95×10^{-9} s^{-1}.

quartz vein and the schist and stress exponent n_q was varied between 1.0 and 4.0. In order to maintain the viscous-brittle strength ratio $R^q = \tau_v^q/\tau_f^q = 1.2$ in the quartz (cf. Section 5.5), i.e., to maintain the same overall viscous strength in the quartz vein of 60 MPa, we adjusted A_M-values for different stress exponents n_q according to Eq. (2) (Fig. 12; see also Kenis et al., 2004). The schist was chosen to be fully brittle again so that this model series corresponds to cases A–C in Fig. 7.

Fig. 13 shows the results of the model runs at 2.5 cm and at 5.0 cm total displacement. Perhaps surprisingly, the stress exponent has little influence on the deformed shape of the quartz vein. For $n_q = 1.0$ and 2.0, the subtle differences in the shapes of the quartz veins in Fig. 13 arise from incipient broadening or bifurcation of the brittle fault in the schist (Section 5.4). The reason for this insensitivity to n_q is that, under the chosen conditions, with relatively uniform quartz strength (effective viscosity), the shape of the deformed veins is predominantly controlled by the higher viscous strength of the enclosing wall rock material (the schist), rather than by the stress exponent of the vein material (cf. Section 5.7).

Table 4
Model parameters for model series 4.

A_M^s (MPa^{-n} s^{-1})	V^{qs}	$R^s = \tau_v^s/\tau_f^s$
1.25×10^{-16}	0.8	1.5
3.94×10^{-17}	0.6	2.0
1.91×10^{-17}	0.5	2.4
7.80×10^{-18}	0.4	3.0
2.48×10^{-18}	0.3	4.0

5.7. Results – model series 4: influence of the quartz-to-schist viscous–viscous strength ratio $V^{qs} = \tau_v^q/\tau_v^s$ on the deformed vein shape

Since the schist is sometimes observed to have been deformed viscously as well as brittlely (e.g., in step-over zones between two adjacent faults, or at deeper structural levels towards the bottom of the shear array), in this section, we investigate the influence of a schist that can also deform viscously.

In this series of experiments, we maintained a 2 cm thick horizontal quartz vein with a power law rheology for all models of this section ($n_q = 4.0$, $A_M^q = 3.06 \times 10^{-16}$ MPa^{-n} sec^{-1}). In addition, the wall rock schist was assigned a power law rheology with $n_s = 4.0$. For the schist, different values of A_M^s were used in a series of experiments, resulting in different viscous-to-brittle strength ratios in the schist (R^s) as is summarised in Table 4.

From a plot of the modelled width of ductile shearing (*dsw*) inside the quartz veins against the magnitude of ductile displacement (*d*) across the shear (Fig. 14a), we conclude that the ductilely sheared width in the quartz veins is sensitive to the quartz-to-schist effective viscosity ratio V^{qs}. The stiffer the schist, i.e., the lower the ratio V^{qs}, the narrower is the *dsw* in the enclosed quartz vein. This relationship follows a power law for all values of V^{qs}. There is a decrease in the gradient of the curves for decreasing values of V^{qs}.

We compared our modelling results for the 2 cm thick vein models with the subset of our field data embracing veins that have

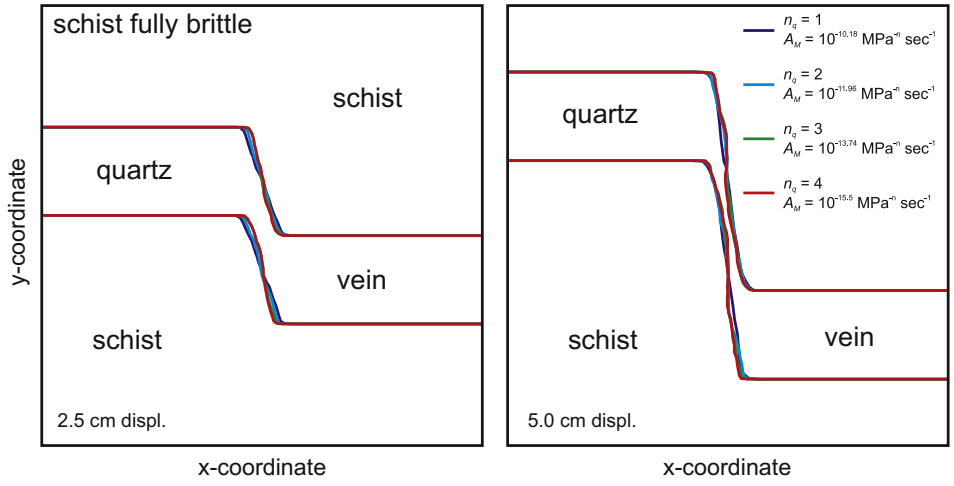

Fig. 13. Modelling results of series 3 – Shape of deformed quartz veins for different stress exponents at total displacements of 2.5 and 5.0 cm. Note the remarkably similar shape of all four veins.

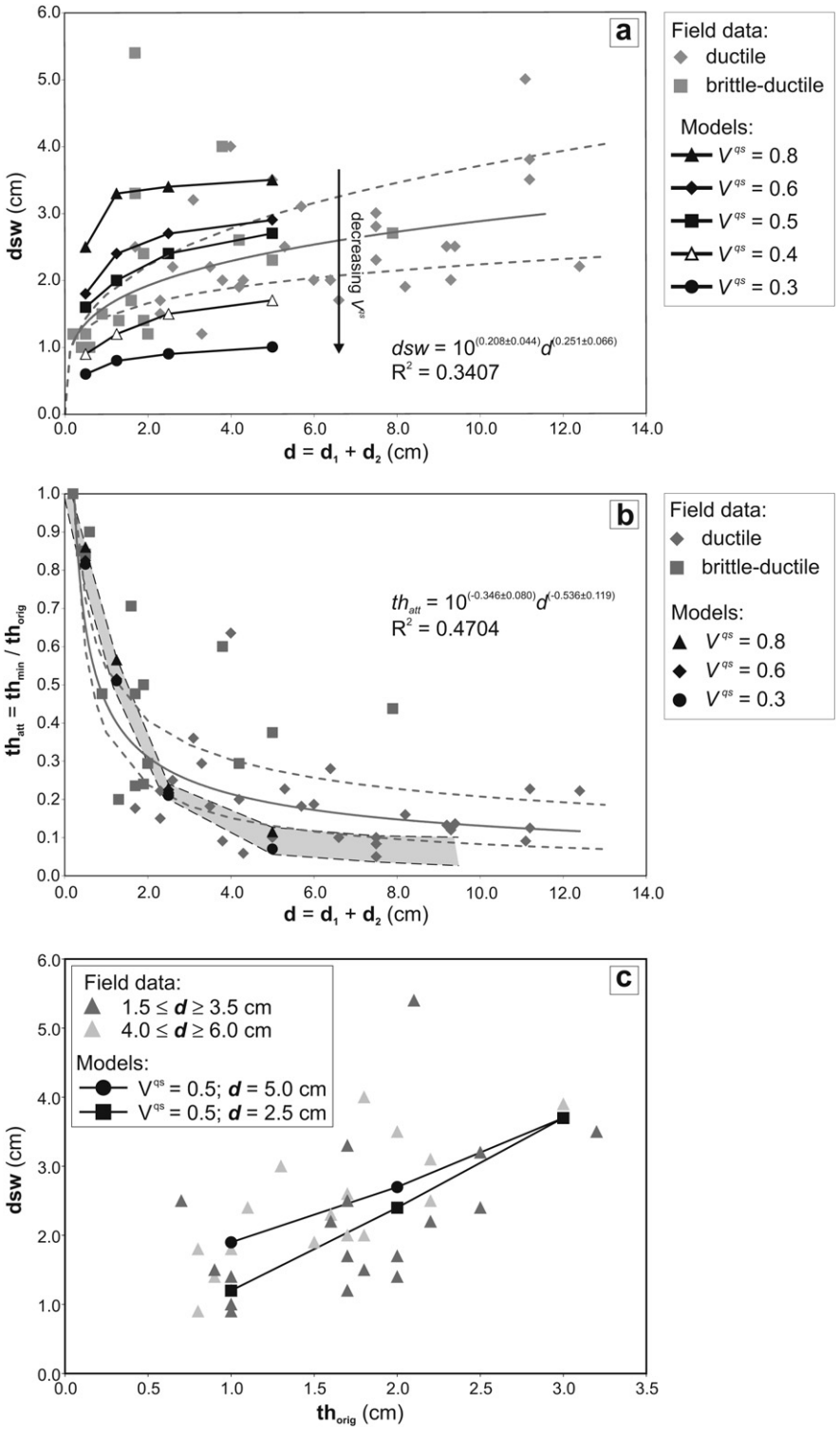

Fig. 14. Results of model series 4 – viscosity ratio of schist and quartz. a) Ductilely sheared width (*dsw*) versus ductile component of slip ($d = d_1 + d_2$) for model vein with $th_{orig} = 2$ cm. The field data (grey) is plotted for veins with original thicknesses between 1.5 and 2.5 cm -and is best bracketed by the curves for $0.4 \leq V^{qs} \leq 0.6$. b) Vein attenuation (th_{att}) versus ductile component of slip (d). It is not possible to clearly discriminate between the results for vein attenuation under different V^{qs}. The range of th_{att} values from the computer models is indicated by the grey shaded area. Dashed lines correspond to the errors calculated for the trendlines. c) *dsw* versus th_{orig}. Results for $V^{qs} = 0.5$; i.e., the schist host rock is twice as viscous as the quartz veins. Slope of linear relationship between *dsw* and th_{orig} depends on the total amount of ductile displacement (d). Measurement uncertainties are ± 0.2 cm.

a thickness between 1.5 and 2.5 cm. When the modelling predictions are compared to the field data, the two model-based curves that best envelope the corresponding field data are those for V^{qs} -ratios of 0.4 and 0.6, that is, where the effective viscosity of the schist is 2.5–1.6 times greater than that of the quartz vein. We also plotted the degree of vein thinning th_{att} versus the ductile slip (d). However, this parameter seems less useful, as all V^{qs} values seem to fit the field data approximately (Fig. 14b).

From the field data presented in Section 4, we inferred that there is a positive scaling relationship between the original vein thickness th_{orig} and the ductile shear zone width (*dsw*). Above, we argued that the best estimate of V^{qs} is 0.5, i.e., the effective viscosity of the schist is 2 times greater than that of the quartz. This result is particularly interesting, because prior to shearing, most veins have been boudinaged and/or folded about the Alpine foliation (Little et al., 2002a, b) indicating that they once had a higher effective viscosity than the surrounding schist. $V^{qs} = 0.5$ therefore implies a reversal of the viscous strength ratio between quartz and schist sometime prior to their late Cenozoic shear deformation (Grigull, 2011).

As a final set of experiments, we modelled the shear deformation of the quartz veins across a range of original vein thicknesses of 1.0, 2.0, and 3.0 cm with that V^{qs} -ratio. For these models we did not allow the quartz veins to yield brittlely. Fig. 14c shows the comparison of the modelling results at 2.5 and 5 cm total displacement. The field data was divided into two groups of ductile slip: a) 1.5–3.5 cm and b) 4.0–6.0 cm in order to make the modelling results comparable to the field data. The modelling results fit well within the field data and both suggest that there is a linear relationship between th_{orig} and *dsw*.

6. Discussion

6.1. Shear bifurcation, energy dissipation, and brittle-viscous coupling between schist and quartz

Since the majority of the surveyed fault-vein sets show that the faults are either nearly straight or bend around the outside margins of the sheared quartz veins, we can infer from model series 1 that the viscous-to-brittle strength ratio between viscous quartz and brittle schist (respectively) must have been close to 1 ($R^{qs} = 1.2$) or slightly higher ($R^{qs} = 5.0$); that is, very nearly balanced. Additionally, in the field we only observed a single fault close to each sheared vein. We were only able to simulate a single fully localised fault propagating towards the quartz vein without bifurcating for a viscous-brittle strength ratio of $R^{qs} = 1.2$.

The difference in fault bifurcation and propagation behaviour between the models with a linear quartz viscosity (L-models) versus those with a power law quartz rheology (P-models) can be understood by considering the effects of energy dissipation minimisation. Both brittle and viscous energy dissipation rates increase with increasing strain rate, most markedly for non-linear viscous materials. To reduce the dissipation rate in the flowing quartz, deformation may become more spread out or diffuse, a relationship that can encourage bifurcation of shears in the adjacent schist. For example, for the same imposed boundary slip rates and flow stress in the linear vs. power-law model (e.g., a flow stress of 60 MPa, Fig. 12), it can be shown that to obtain the same rate of viscous energy dissipation, a lower viscous strain rate is needed for the linear flow-law case. A reduction in strain rate can most easily be attained by widening the ductile shear width. The statements above follow from the observation that viscous energy dissipation rate (per unit volume) in a power law material is proportional to the strain rate and depends on the stress exponent:

$$\dot{w}_v \propto \dot{\varepsilon}_s^{1+1/n} \tag{5}$$

(e.g., Malvern, 1969, p. 300), where $\dot{w}_v$ is the viscous energy dissipation rate, $\dot{\varepsilon}_s$ is shear strain rate, and n is the stress exponent. Fig. 15 depicts the physical meaning of Eq. (5) schematically: where $n > 1$ an increase in strain-rate causes a lesser increase in energy dissipation rate compared to the equivalent case with lower stress exponent ($n = 1$).

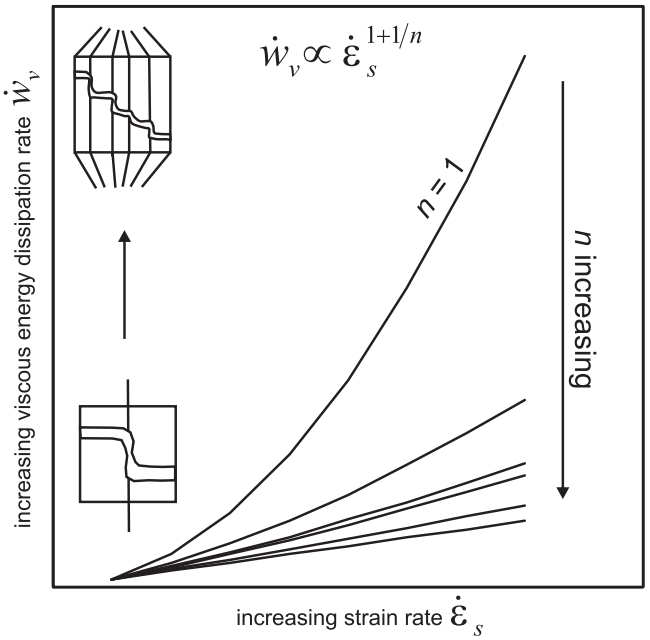

Fig. 15. Viscous energy dissipation rate $\dot{w}_v$ versus shear strain rate$\dot{\varepsilon}_s$. $\dot{w}_v$ is slower for higher stress exponents n. More brittle faults form for higher dissipation rates. The biggest difference in energy dissipation rate is between $n = 1$ and all stress exponents that are higher than 1. This explains the discrepancies between the L- and the P-models in Section 5.4.

Considering an isolated shear with a constant yield strength in the schist, the total frictional (i.e. brittle) energy dissipation rate (per unit volume) is linearly proportional to the strain rate $\dot{\varepsilon}_s$ and depends on the shear stress τ:

$$\dot{w}_f \propto \tau \cdot \dot{\varepsilon}_s \tag{6}$$

where $\dot{w}_f$ is the frictional (i.e. brittle) energy dissipation rate. The bifurcation of one shear results in two shears that each move at only half of the total strain rate. In other words, the brittle dissipation rate per shear also depends on the number of shears (N_{shears}) that form ($\dot{w}_f \propto \tau \cdot \varepsilon_s / N_{\text{shears}}$). This is a way to reduce the energy dissipation in the schist on one shear. Integrated over the whole volume, however, the brittle energy dissipation rate for the same system split into two or many shears is the same, so that there is no inherent tendency of a brittle material to localise (e.g., Buiter et al., 2008). It is only with the imposition of strain softening that localisation of brittle shearing onto one through-going shear becomes favoured (Huismans et al., 2005). Since the schist is inferred to be a strain-softening brittle material, the lowest energy configuration for the schist after softening has occurred and at high strain rates will be along narrow and strongly localised shears or faults (e.g., Huismans et al., 2005). Therefore, a competition exists between the "lowest energy dissipation configuration" for ductile vs. brittle materials; that is, localisation in the brittle schist and diffuse deformation in the viscously shearing quartz.

For the brittle-viscously coupled quartz vein-fault sets in the Southern Alps, the brittle and viscous energy dissipation rates must have been nearly equal, since the faults that offset the quartz veins are very well localised (and they do not bifurcate in the vicinity of the quartz veins). This energy balance is also reflected in the modelling results: as we found that it was possible to achieve fault localisation from the earliest stages of deformation when the viscous-brittle (quartz-schist) strength contrast R^{qs} was close to 1. These results are supported by the numerical model series of Schueller et al. (2005, 2010) who found that it is possible to achieve plastic strain localisation in a brittle material bracketed by two

ductile layers for low to medium viscosities of the ductile material. An R^{qs} -ratio of ~1 in our models would correspond to a viscosity of ~100 in the models of Schueller et al. (2005); the upper end of their "viscosity-dependent mode".

6.2. Brittle-ductile transition in quartz veins

Compared to the field data in Fig. 5c and d, the numerical models with the brittle-viscous strength ratio $R^q = 1.2$ for quartz best simulate the scaling relationships observed in the field. Fig. 5c, d showed that the D-ratios of the majority of the veins with a brittle slip component lie below 0.5. The models in Section 5.5 may provide one reason for this behaviour. We showed that there are two paths to producing vein displacements that are both brittle and ductile: a) distributed ductile deformation of thick veins first, leading to extreme attenuation of a quartz vein, which leads to brittle failure of that vein; or b) localised brittle failure of thinner veins first, followed by ductile shearing of the quartz vein in the areas of reduced strain rates that are away from the central shear zone. The question remains whether the brittle faults formed first or whether the distributed ductile shearing was first. If we assume that both failure sequences could have been present in the quartz veins, we can argue that $R^q = 1.2$ is the best estimate for these quartz veins.

We can explain that $D < 0.5$ for most of the brittle-ductile quartz veins by assuming that brittle slip continued to accumulate after brittle failure of the quartz veins. Soon after brittle failure of a quartz vein, ductile slip (d) ceases whereas the total slip (y_{tot}) continues to increase by brittle slip. Since $D = d/y_{\mathrm{tot}}$, this results in the ductility D asymptotically approaching zero with increasing y_{tot}. If this hypothesis proves true, y_{tot} was high enough compared to d to result in $D < 0.5$ for most brittle-ductile quartz veins in the study area.

6.3. Stress exponent in the quartz veins

Following the work of Talbot (1999) and Kenis et al. (2004), one might expect the shape of the quartz veins (in particular the ductile shear zone width) to carry information about the stress exponent and therefore also about the deformation mechanism. For example, if the model shapes using $n_q = 1$ fit those observed in the field, then we would infer that the veins were probably deformed by diffusion creep or dissolution-precipitation creep. By contrast, if $n_q >> 1$, we would conclude that the main deformation mechanism prior to static recrystallisation was dislocation creep (cf. Section 1).

However, the models in series 3 suggest that even if there were a change in deformation mechanism, the shape of a quartz vein will not reflect this transition because as shown in Fig. 13, the stress exponent (e.g., $n_q = 1$ or $n_q = 4$) in the quartz does not significantly influence the shape of the sheared vein as long as the surrounding schist is stronger than the quartz. Talbot (1999) investigates shear zones in homogeneous, fully viscous materials, whereas our models include two materials (quartz and schist) with two different mechanical behaviours (viscous vs. brittle). Our data reveal that as soon as there is some brittle behaviour involved in the shearing of a transverse marker, the relationship between n and shear zone width (dsw) and deformed marker shape is no longer simple.

6.4. Viscosity contrast between schist and quartz

The quartz veins in our study area are typically deformed in a ductile way, whereas the schist is brittlely displaced across narrow faults. This leads to the conclusion that the schist was viscously stronger than the unfaulted quartz veins embedded within it. The stiffer schist reacted to the brittle yield criterion whereas the softer, flowing quartz veins did not. Although under certain conditions, the schist reacted ductilely to the shearing (Section 5.1, Fig. 6). In Section 5.7 we showed that the final shape of a deformed quartz vein seems to mainly depend on the viscosity contrast between quartz and schist. We were able to constrain the viscosity ratio between quartz and schist to $0.4 < V^{qs} < 0.6$. This means that the schist had approximately twice the flow strength of the quartz veins during shearing. This strength contrast is small, in agreement with other field-based rheological studies that inferred viscosity contrasts of 1–10 between quartz and psammite materials (e.g., Treagus, 1999; Treagus and Treagus, 2002; and references therein; Kenis et al., 2004). We have shown that, even at a small viscosity contrast between schist and quartz vein, the rheology of the stronger material (schist) controls the resulting shape of the weaker material (quartz).

6.5. Estimation of quartz flow parameters constrained by modelling

The determination of the viscous-to-brittle strength contrasts of ductile quartz and brittle schist and of viscosity ratios of those two rock materials enables us (under certain assumptions) to calculate a minimum and maximum pre-exponential factor A_E for the quartz veins across the full range (maximum and minimum) of possible mean slip rates for the shear array (cf. Section 4). Based on a Griffith-Mohr-Coulomb failure criterion, we assumed a minimum brittle yield strength in the quartz veins and the schist of $\tau_f^q = \tau_f^s = 50$ MPa (Grigull, 2011). Using the previously determined viscous-to-brittle strength ratios that best fit our field data ($R^{qs} = \dfrac{\tau_v^q}{\tau_f^s} = 1.2$, and $R^q = \dfrac{\tau_v^q}{\tau_f^q} = 1.2$), we calculate from our models and field data a best-fit viscous quartz flow strength of $\tau_v^q = 60$ MPa. The minimum slip rate estimate for the brittle-ductile shears was 1.4×10^{-4} mm/yr and the maximum estimate was 2 mm/yr resulting in natural (=model) shear strain rates of 2.7×10^{-12} s^{-1} and 3.18×10^{-8} s^{-1} in the shears respectively (Appendix A). Assuming a stress exponent $n_q = 4$ and inserting those values into Eq. (2) gives $A_M = 2.08 \times 10^{-19}$ MPa^{-n} s^{-1} for the slowest (all shears active) and $A_M = 2.45 \times 10^{-15}$ MPa^{-n} s^{-1} for the fastest strain rate (one shear active). In a triaxial deformation experiment, the calculated natural minimum and maximum shear strain rates would correspond to 3.12×10^{-12} s^{-1} and 3.67×10^{-8} s^{-1}. Excluding water fugacity, these strain rates would result in $A_E \approx 10^{-12}$ MPa^{-n-m} s^{-1} and $A_E \approx 10^{-8}$ MPa^{-n-m} s^{-1}.

We are able to derive a flow law for quartz from a) the interaction between brittle faults and quartz veins that have been ductilely-to-brittlely offset across those faults, and b) geometrical scaling relationships in those sheared quartz veins:

$$\dot{\varepsilon} = 10^{-10 \pm 2} \cdot f_{\mathrm{H_2O}} \cdot \sigma_d^{4.0} \cdot \exp\left(\frac{135\ \mathrm{kJ\ mol^{-1}}}{\mathrm{RT}}\right) \quad (7)$$

In Fig. 16, we plotted this flow law using a geological strain rate of $\dot{\varepsilon} = 1.0 \times 10^{-14}$ s^{-1}. For comparison, we also plotted the laboratory-derived flow law of Luan and Paterson (1992) and the partly geologically derived flow law of Hirth et al. (2001). These flow laws are frequently used to describe the viscous behaviour of the Earth's crust. The flow law that resulted from this study and the ones by Luan and Paterson (1992) and Hirth et al. (2001) all have a stress exponent of $n = 4.0$. Luan and Paterson's as well as Hirth et al.'s flow laws predict $Q = 135$ kJ mol^{-1}, which we adapted for our models so we can directly compare them. Fig. 16 shows that our results bracket the flow laws by Luan and Paterson (1992) and Hirth et al. (2001). We therefore conclude that the computer models (and the assumptions contained within them) are in reasonable

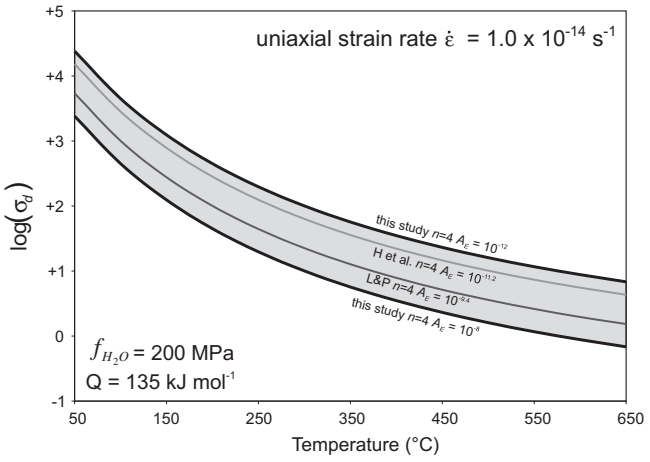

Fig. 16. Differential stress versus temperature using Eq. (1) with the flow law parameters that were derived for the quartz veins in this study. Plotted for a natural strain rate of 1.0×10^{-14} s^{-1}. Flow laws of Hirth et al. (2001) and Luan and Paterson (1992) are shown for comparison. Grey shaded area indicates the range of differential stresses that are possible with our flow law parameters at that fixed strain rate. A_E = pre-exponential factor; n = stress exponent for quartz.

agreement with extrapolations of experimentally derived flow laws to natural strain rates. Although we confirm that experimentally derived flow laws for quartz are applicable to the quartz veins in our study area, they may not be valid for quartz in the highly strained rocks of the Alpine Fault mylonite zone, where the deformational history and the preservation of an early high temperature fabric in these mylonites influenced the later flow behaviour and development of the final CPO (e.g., Toy et al., 2008).

7. Conclusions

By comparing numerical models to field-based scaling relationships measured in ductilely to brittlely sheared quartz veins, we have derived two important ratios describing the effective rheology of natural quartz veins: (1) the viscous-to-brittle strength ratio between ductile quartz veins and brittle host schist $R^{qs} = \tau_v^q/\tau_f^s$ must lie between 1.0 and 5.0, in order to form a single localised fault that bends around the margin of the deforming quartz vein rather than cutting across the vein. (2) the quartz to quartz viscous-to-brittle strength ratio ($R^q = \tau_v^q/\tau_f^q$) needs to be between 1.2 and 1.4, to allow the models to reproduce field observations that veins with original thicknesses greater than 2 cm commonly remain partly to fully unbroken or ductile up to a displacement of ~7.5 cm, whereas veins of less than 2 cm thickness commonly are fractured and include a significant brittle component of slip.

Because of the brittle-ductile nature of the deformation, it is not possible to use the macroscopic deformed shape of the sheared quartz veins by itself to infer the stress exponent for the quartz veins. However, in our numerical models, we were only able to attain planar fault localisation at the fault-quartz vein intersection (as observed in the field) when that quartz vein had a power law stress exponent of $n_q = 4$. We assume therefore that n_q was probably closer to 4 than to 1. This means that the quartz veins in our study area probably deformed by dislocation creep rather than diffusional or dissolution-precipitation processes. We further conclude that viscous quartz bodies may control the propagation and bifurcation behaviour of faults in an otherwise purely brittle schist.

We were able to use the scaling relationship between ductile shear zone width in the quartz vein and ductile displacement of the quartz vein to deduce a viscosity ratio between the quartz veins and the surrounding host schist. In an environment where the schist may deform viscously as well as brittlely, the viscosity contrast V^{qs} between quartz and schist seems to be the major control on the final shape of the sheared quartz veins. Our models suggest that the schist host is about twice as viscous as the quartz veins embedded in it ($0.4 \leq V^{qs} \leq 0.6$).

Using the viscous-to-brittle and viscous-to-viscous strength ratios between quartz and schist, and assuming a minimum brittle yield strength for the schist and the quartz, as well as a stress exponent of 4 for the quartz, we are able to calculate a range of pre-exponential factors that fit our field data well. This set of flow law parameters are consistent with published experimentally derived flow laws.

Acknowledgements

For their help during field work and for fruitful discussions about the fault array we would like to thank E. Schermer, J. Onnecken, R.Wightman and K. Peters. We acknowledge funding for S. Grigull from a Vice-Chancellor's strategic research scholarship from Victoria University of Wellington. S. Ellis was supported by GNS Science's Direct Crown Funded Programme, "Tectonics and Structure of Zealandia". E. Dempsey and S.J. Covey-Crump are thanked for their thorough reviews and highly valuable comments that helped to improve the manuscript. We thank R. Holdsworth for the editorial handling.

Glossary

$\dot{\varepsilon}, \dot{\varepsilon}_S$	uniaxial strain rate, shear strain rate
σ_d, τ	differential stress, shear stress
τ_v^q, τ_v^s	viscous flow stress in quartz, schist
τ_f^q, τ_f^s	brittle yield stress in quartz, schist
n	stress exponent
A_E	experimentally derived pre-exponential factor
A_M	pre-exponential factor used in models
R^{qs}	ratio τ_v^q/τ_f^s, viscous-to-brittle strength contrast between quartz and schist
R^q, R^s	ratios τ_v^q/τ_f^q, τ_v^s/τ_f^s, viscous-to-brittle strength contrast in quartz, schist V^{qs} ratio τ_v^q/τ_v^s, viscous-to-viscous strength contrast between quartz and schist
y_{tot}	total displacement or slip
b	brittle component of displacement or slip
d	ductile component of displacement or slip ($d_1 + d_2$)
D	ratio d/y_{tot}
dy/dt	differential velocity or total slip rate
$\dot{y}_{min}$,$\dot{y}_{max}$	minimum, and maximum field-based slip rate estimates
dsw	ductilely sheared width
th_{orig}	original vein thickness
th_{min}	minimum vein thickness
th_{att}	attenuation ratio $\mathrm{th_{min}/th_{orig}}$

Appendix A. Detailed derivation of physical constraints in Table 1

A.1. Time available for ductile deformation and subsequent static recrystallisation of the quartz veins

The time available for exhumation of the brittle-ductile fault array is ~3.5–3.8 Myr. This calculation is based on the currently observed ~5–7 km distance of the fault array normal to the Alpine Fault, and assumes that there was no deformational change in the thickness of the exhumed structural section. If the detachment was ~32 km deep (Kleffmann et al., 1998; Stern et al., 2001; Scherwath et al., 2003) then the array was at an original depth of 25–27 km. For a late Quaternary dip-slip rate in the central part of the Alps of

10 mm/yr (Norris and Cooper, 2001) along an Alpine Fault that dips 45° (e.g., Norris and Cooper, 1995), these data imply a maximum exhumational time interval of 1.5 Myr for rocks to be carried from the ramp step to ~10 km depth (Wightman, 2005), where the seismically inferred ~300 °C isotherm is located (Shi et al., 1996; Batt and Braun, 1999) (Fig. 1c). We assume that at temperatures less than 300 °C quartz will cease to deform by crystal plastic creep (e.g., Hirth and Tullis, 1994; Stöckhert et al., 1999). This estimate also includes time for the observed static recrystallisation to be completed. Wightman (2005) used empirical grain growth rate-equations in quartz (after Tullis and Yund, 1982) and calculated the time-interval that was necessary for grain growth from 1 μm (original estimated dynamically recrystallised grain size after shearing using the paleopiezometre of Mercier et al., 1977) to 100 μm (approximate grain size after static recrystallisation) to be ~1 Myr. Subtracting this time-interval from the total available time of 1.5 Myr, the maximum time for vein deformation is only 0.5 Myr.

A.2. Temperature

Several constraints can be placed on the temperature during shearing of the quartz veins. An upper limit for deformation temperature of 600–700° C is given by late Cenozoic metamorphism temperatures in the amphibolite facies rocks closer to the Alpine Fault that structurally underlie the faulted rocks in our study area (Cooper, 1980; Vry et al., 2004). The rocks that host the brittle-ductile faults are greenschist facies rocks in the biotite-zone; however, they do not show any signs of retrogressive metamorphism that may have been associated with late Cenozoic shearing or fluid infiltration. From these observations maximum deformation temperatures of 350–500° C are inferred. Using Titanium-in-quartz geothermometry (Wark and Watson, 2006), Grigull (2011) measured what she interpreted to be minimum estimates of the temperature of static recrystallization of 425 ± 38° C for deformed veins from Chancellor Ridge and 400 ± 21° C for veins from Crawford Knob. For the undeformed parts of the same veins, Grigull (2011) measured minimum recrystallisation temperatures of *c.* 530° C, presumably a relict of the original vein emplacement and static recrystallisation process prior to shearing. Applying the recently established pressure-dependent geothermometer of Thomas et al. (2010) at a lithostatic pressure of 560 MPa (cf. Section A.3) would result in temperatures that are ~20° C lower than the ones derived from the geothermometer of Wark and Watson (2006). After demonstrating isotopic equilibrium conditions, Wightman (2005) performed quartz-calcite oxygen isotope studies on four of the fault-infilling veins to estimate a temperature of 480 ± 50° C for the time of vein deformation. From the TitaniQ and oxygen-isotope geothermometry, we predict a temperature range of 400–530° C at the time of vein deformation. For the geodynamic models presented in this paper we use a mean deformation temperature of 450° C.

A.3. Deformation depth and stress state

Late Cenozoic $^{40}Ar/^{39}Ar$ muscovite cooling (plateau) ages in the host rocks at Crawford Knob of 3.4–4.5 Ma (Wightman, 2005) record the time of cooling of the rocks through ~400 ± 50° C. These ages correspond to temperatures of cooling that are within the lower range of the deformation temperature of the quartz veins. The late Quaternary dip-slip rate on the Alpine Fault (10 ± 2 mm/yr, Norris and Cooper, 2001) and the dip of the Alpine Fault (45°) can then be used to calculate the minimum depth of exhumation of those rocks of ~28 ± 7 km.

Petrologically based estimates for the exhumation depth of rocks currently exposed in the mylonite zone at the Alpine Fault are 25–35 km (e.g., Norris and Cooper, 2003; Vry et al., 2004; Toy, 2007). Seismic reflection data suggests a detachment depth of >32 km for the Alpine Fault (Kleffmann et al., 1998; Stern et al., 2007). Since the faulted rocks that are exhumed at Crawford Knob lie 5–7 km structurally above the mylonites of the Alpine Fault, these data imply an original depth of 20–30 km for the faulted array. In this paper, we assume a minimum depth of shear zone formation of 21 km, which leads to an inferred minimum overburden pressure of $P_{lith} \approx 560$ MPa (assuming a rock density $\rho = 2700$ kg/m^3 and $P_{lith} = \rho g z$).

Wightman (2005) interpreted microstructures (relict quartz grains with elongate shape and crystallographic preferred orientations at high angles to the faults) in the dilative fault-infilling veins as indicators of original vein emplacement through crack-seal processes into hybrid extensional-shear fractures in the quartz-ofeldspathic rocks, although the relative timing of dilative and shear displacements on the fractures is unclear. Using a combined Mohr-Coulomb-Griffith analysis of brittle fracture for intact rock, a minimum estimate for the differential stress at the time of brittle failure of the host schist is $\sigma_d = (\sigma_1 - \sigma_3) = 100$ MPa, independent of depth or fluid pressure (Wightman, 2005; Grigull, 2011). To cause brittle failure at 21 km depth, such a differential stress would have required pore fluid pressures that were near lithostatic ($P_f = 500$–530 MPa) at the time of brittle failure. Since entrapment fluid pressure of primary aqueous fluid inclusions in the fault-infilling veins was estimated by Wightman (2005) to have been $P_f \geq 310 \pm 90$ MPa (i.e., $\lambda = 0.39$–0.71), we infer that the fluid pressure must have fallen post-failure to near-hydrostatic values. At the entrapment P_f, the expected differential stress for conditions of brittle failure would have been ~340 ± 90 MPa.

A.4. Fault slip rates

Grigull and Little (2008) developed a graphical-algebraic method to project outcrop traces of cylindrically curved veins into the fault movement plane, defined as the plane that contains the slip vector and the pole to the fault plane. Once the vein traces have been projected into the movement plane, the 'true' vein shape and amount of slip in those veins as observed on that plane can be measured. We traced 29 vein-fault sets from Chancellor Ridge and 43 sets from Crawford Knob from the outcrop surface onto transparencies and applied the projection method of Grigull and Little (2008) to those sets. The method requires knowledge of the direction of slip on the fault planes. Based on 101 slip lineations measured on exhumed fault planes at Crawford Knob and 9 at Chancellor Ridge, we measured average slip vectors that pitch 36 ± 11°SW and 30 ± 11°SW, respectively. These agree with Wightman (2005) who calculated a mean slip vector pitch of 36° ± 5° SW for the entire fault array based on an analysis of both fault surface lineations and a detailed analysis of the cutoff-orientations and outcrop separations of the marker veins.

Maximum and minimum estimates of slip rates for the shears can be obtained using the method of Wightman and Little (2007). As one end-member, we apply the kinematic "escalator" model that assumes sequential activation of individual shears through repeated and systematic slip on the faults (Fig. A.1). We used the average spacing ($S = 37 \pm 54$ cm) between the shears at both field locations (Table A.1), as well as the known plate boundary-normal convergence rate $v_{normal} = 10 \pm 1.5$ mm/yr, (NUVEL-1A model of De Mets et al., 1990, 1994; Norris and Cooper, 2001) to calculate the average time during which an individual shear would be active:

$$dt = \frac{S}{v_{normal}} \tag{A.1}$$

where dt is the time necessary for one active shear to move across the distance S (spacing) at the velocity v_{normal} and subsequently become inactive. Based on this extreme assumption that only one shear was active at a time (sequential activation), the average 'life-span' for the shears is $dt \approx 37 \pm 54$ years. Dividing the average total slip $y_{tot} = 72 \pm 58$ mm (Table A.1) by dt results in a maximum estimate for the slip rate of $\dot{y}_{\max} = y_{\text{tot}}/dt \approx 2 \pm 3$ mm/yr 2 ± 3 mm/yr.

At the other extreme, a minimum estimate for the slip rate can be made by assuming that not only one shear was active at a time but that all shears were active simultaneously across the 2 km width of the entire shear array W_{array} (Fig. A.1). This model assumes that $S = W_{array}$. Using Eq. (A.1) with $S = 2$ km and the same plate boundary-normal velocity of 10 ± 1.5 mm/yr results in $dt = 200 \pm 30$ kyrs and thus in a minimum slip rate of $\dot{y}_{min} = y_{tot}/dt \approx (3.6 \pm 2.9) \times 10^{-4}$mm/yr.

In the numerical models, we use a slip rate of $y_{tot}/dt = 0.5$ mm/yr. This modelling slip rate falls between the maximum and minimum bounds outlined above, which are based on end member kinematic models for shear activation and deactivation (only one shear active at a time, sequential activation; all shears slipping together, simultaneous activation). It is 4 times less than the average calculated value of the maximum slip rate (escalator model) and ~1400 times more than the range of minimum slip rates derived from the model that assumes $S = W_{array}$ and from the model based on the estimate of maximum time available for deformation ($1.4–3.6 \times 10^{-4}$ mm/yr). The actual chosen slip rate does not matter for most of our numerical models since we are mostly dealing with viscosity and stress ratios rather than absolute values (Section 5).

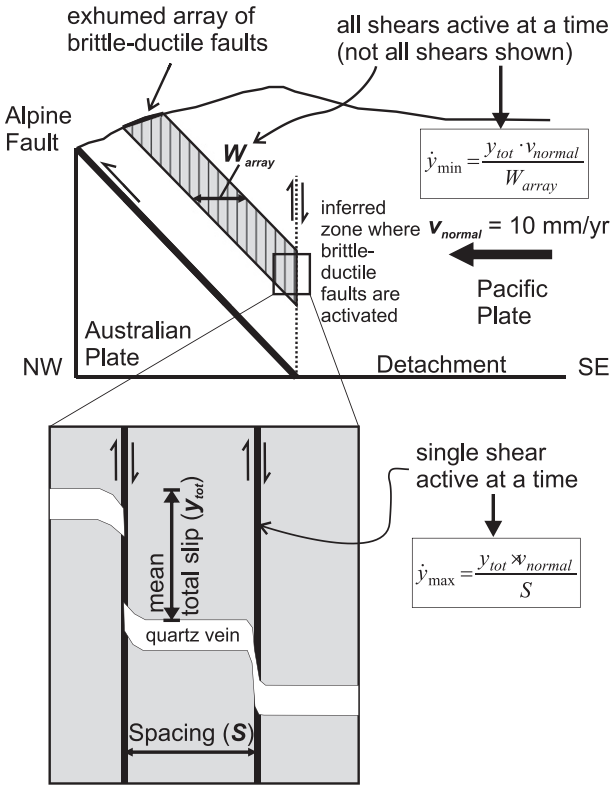

Figure A.1. Variables needed to calculate minimum and maximum slip rates $\dot{y}_{min}$ and $\dot{y}_{max}$ for the brittle-ductile faults (see main text). v_{normal} is plate-normal convergence rate based on NUVEL-1A model by De Mets et al. (1990, 1994), S is the spacing between two adjacent shears, W_{array} is the width of the entire fault array (corresponds to $S = 2$ km).

Table A.1
Field based maximum slip rate estimates, based on the escalator model of sequential shear activation (one shear active at a time) and using the method by Wightman and Little (2007).

Location	Number of shears measured	Mean fault spacing S	Mean slip per fault y_{tot}	Predicted time of shear activity dt	Max. slip rate $\dot{y}_{max} = y_{tot}/dt$
Chancellor Ridge	29	230 ± 260 mm	83 ± 42 mm	23 ± 26 yrs	4.0 ± 5.0 mm/yr
Crawford Knob	43	510 ± 480 mm	62 ± 39 mm	51 ± 49 yrs	1.3 ± 1.5 mm/yr
Average		370 ± 544 mm	72 ± 58 mm	37 ± 54 yrs	2.0 ± 3.3 mm/yr

An alternative way to estimate fault slip rate simply divides the mean slip per fault (~72 ± 58 mm) by the above mentioned maximum limit on the duration of ductile vein deformation (0.5 m.y., Section A.1). This analysis yields a minimum slip rate of $(1.4 \pm 1.1) \times 10^{-4}$ mm/yr. This is a minimum slip rate because it assumes constant and continued activity on the fault throughout its residence in the brittle regime.

Appendix B. The choice of initial flow law for the quartz veins

Wightman et al. (2006) and Hill (2005) have investigated crystallographic preferred orientations (CPOs) in the deformed quartz veins at the studied sites of Crawford Knob and Chancellor Ridge. They have described the CPOs as being very weak to random. This is surprising considering the observed high shear strains of 5–15. The

model for the deformation of these quartz veins by Wightman et al. (2006) suggests a late increment of diffusion creep-accommodated grain boundary sliding which weakened or randomised a pre-existing CPO in the veins. Diffusion creep is a grain size sensitive flow mechanism and usually implies low differential stresses and a small grain size. To our knowledge, diffusion creep in quartz has only been detected and described in the deformation experiments of Brodie and Rutter (2000) and Rutter and Brodie (2004a) which were performed on ultrafine grained (< 4.5 μm) aggregates. The model of Wightman et al. (2006) essentially describes three stages in the deformation of the veins: a) grain-size reduction through dynamic recrystallisation (i.e., dislocation creep) during shearing of the rocks, b) a stress-drop once the shearing stopped, i.e., once the rocks have passed the foot of the Alpine Fault ramp, c) grain growth through static recrystallisation while the rocks are being shifted upwards along the ramp. Small grain sizes after phase a) and the waning differential stress in b) may have induced a change in deformation mechanism from dislocation creep to diffusion creep-accommodated grain boundary sliding and hence randomisation of the CPO.

In order to preselect an initial flow law for input into the numerical models (Section 5.3.2.) we have investigated several published grain size sensitive (GSS) and grain size insensitive (GSI) flow laws as well as grain size – stress relationships (paleopiezometers) for quartz against the background of the geological setting of the Southern Alps (inset in Fig. B.1a). For these models we assumed an Alpine Fault dip of 45°, a convergence rate of 10 mm/yr and a temperature gradient of ~21° C/km (resulting in a temperature of 450 °C at 21 km depth; Fig. B.1a). In agreement with the entrapment fluid pressure that was measured in primary fluid inclusions in the shear-infilling veins (~310 MPa, cf. Section A.3. and Wightman, 2005), the ratio fluid pressure to lithostatic pressure was set to $\lambda = 0.6$ (Fig. B.1a). It was also assumed that the a time period of 0.5 Myr through 1) a grain size independent dislocation creep flow law, and 2) a grain size dependent diffusion creep flow law. We used the dislocation creep flow law of Hirth et al. (2001), the diffusion creep flow law of Brodie and Rutter (2000) and the paleopiezometer of Stipp and Tullis (2003) in order to investigate the contribution of GSI and GSS flow to the accumulated shear strain. Table B.1 summarises the parameters that were used to calculate strain rates and accumulated strains.

Table B.1
Flow law parameters that were used to calculate accumulated strain by GSS and GSI processes. For the calculation of A_M, see Eq. (3).

	Equation (cf. Eqs. (1) and (4))	A_E (MPa^{-n} s^{-1})	n	r	Q (kJ/mol)
GSI flow law (Hirth et al., 2001)	$\dot{\varepsilon}_s = A_M \tau^n \exp(-Q/RT)$	6.31×10^{-12}	4.0	–	135
GSS flow law (Brodie and Rutter, 2000)	$\dot{\varepsilon}_s = A_M \tau^n \exp(-Q/RT) d_g^{-r}$	0.631	1.0	2.0	220

	Equation	A (MPa μm$^{-1/m}$)	k
Palaeopiezometer (Stipp and Tullis, 2003)	$d_g = A\sigma_d^{-k}$	3630.78	1.26

Since both flow laws include a water fugacity term, and since water fugacity is temperature and pressure dependent, we used a "water fugacity calculator" that is available on a webpage by the University of Minnesota (http://www.geo.umn.edu/people/researchers/withe012/fugacity.htm) on the equation by Pitzer and Sterner (1994), in order to calculate the water fugacities for these temperature and pressure values.

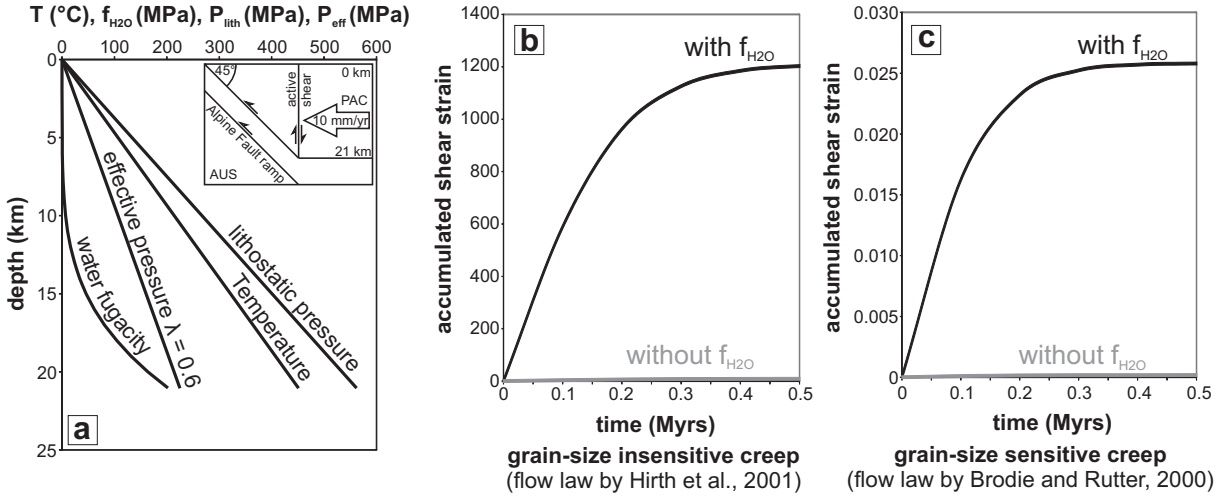

Figure B.1 a) Simplified PT-conditions that could have prevailed during the activity of a shear. We also plotted water fugacity according to the changes in pressure and temperature following the equation of Pitzer and Sterner (1994). Inset: kinematic setting in the Southern Alps that was used to calculate pressures, temperatures and strain rates. b) Shear strain that was accumulated by grain size insensitive power law creep during 0.5 Myr of shearing under changing water fugacity, temperature, and effective pressure conditions. c) Shear strain that was accumulated under the same conditions as (b) but by grain size sensitive creep (linear creep law) also in 0.5 Myr. Note that in (c), 47,000 times less shear strain than in (b) is accumulated.

escalator model of Little et al. (2002a) could be used to simulate the evolution of the brittle-ductile fault array, and that only one shear was active at a time and that shearing continued until this shear reached the surface (depth = 0 km).

In order to justify the choice of a dislocation creep flow law as input into the numerical models (main text), we demonstrate how different the amounts of shear strain are, that are accumulated over

The graphs in Fig. B.1b, c show clearly that the GSI accumulated shear strain is approximately 47,000 times higher than the shear strain that was accumulated by GSS creep. The maximum shear strain that is achieved by grain size sensitive creep is ~0.026 using the paleopiezometer by Stipp and Tullis (2003) to calculate the corresponding grain sizes. The fraction of shear strain that is contributed to the total accumulated shear strain by GSS creep is

therefore negligible. To match our field data, we would have required a shear strain of at least 2.

We therefore conclude that even if diffusion creep-accommodated grain boundary sliding had been active at some stage in the deformation of the veins, it barely contributed to the high strains in the veins, and would therefore not affect the deformed vein shapes observed in the field. We further conclude that GSI dislocation creep seems to be the dominant deformation mechanism during shearing of the veins, and that this deformation mechanism is responsible for the observed high shear strains and deformed vein shapes. We therefore used the GSI power law by Hirth et al. (2001) as an initial flow law input in the numerical models in this study.

Appendix C. Strain softening used in models

In general, the dilative faults that displace the quartz veins and Alpine Schist host rocks are ~2 mm wide, planar, and are inferred to have propagated as discrete fractures through the brittle schist to the quartz veins (Section 5.3.1). Since SULEC is not set up to include dilative material behaviour, we modelled the brittle faults as a frictional-plastic shear zone in the schist. In order to achieve shear zone localisation in the schist in the models, the brittle schist needs to be able to strain soften. We ran four preliminary models (S1–S4) to find a plausible strain softening case resulting in a model that is able to simulate our field observations: a well-formed, narrow, straight, discrete shear (even at mm-scale offset) that has propagated to the quartz vein. In these models we varied a) the total amount of strain softening and b) the strain softening gradient (Fig. C.1). The results of these models show that the strain localisation in the schist depends primarily on the slope of the stress-plastic strain curve (models S1, S2, S4 in Fig. C.1) rather than the total absolute value of the softened yield strength (models S2, S3 in Fig. C.1). The steeper the strain softening gradient is, the more localised and the further propagated is the frictional-plastic shear zone. If the gradient is very steep as in S1, however, the shear is not well localised at the intersection with the quartz vein. For a shallow gradient (S4), the shear has not reached the quartz vein yet after 1 mm of displacement, and deformation is more diffuse than in the other cases. The results for cases S2 and S3 are very similar since both have the same softening gradient. For all the models in the main modelling series (1–4) presented in this paper, we chose softening case S2 (bold line in Fig. C.1), so that the brittle shear zone is fully established after a maximum of 1 mm total displacement corresponding to a plastic strain of ~0.1.

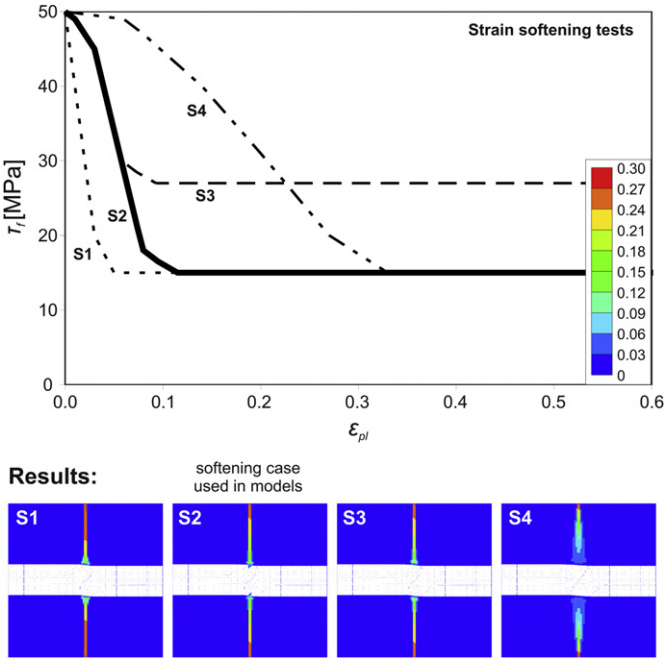

Fig. C.1. Strain softening tests. The graph represents brittle yield stress plotted against plastic strain in a series of experiments. S2 best represents our field observations. Results are contour plots of plastic strain after 2 years of shearing (corresponding to 1.0 mm displacement). Note how the models with the steeper softening gradients have already fully established brittle shear zones whilst the fault zone in the model with the shallower gradient has not propagated to the quartz vein yet.

Appendix D. Strain rate conventions in SULEC

SULEC reports shear strain (and shear strain-rate) as:

$$\dot{\varepsilon}_s = \frac{1}{2}\left(\dot{\varepsilon}_{ij} + \dot{\varepsilon}_{ji}\right) \tag{D.1}$$

For example, consider the shear strain rate near the upper boundary of a model where a differential velocity V, is applied across a total length dl. SULEC will report the shear strain rate as:

$$\dot{\varepsilon}_s = \frac{1}{2}\left(\dot{\varepsilon}_{ij} + \dot{\varepsilon}_{ji}\right) = \frac{V}{2dl} \tag{D.2}$$

Appendix E. Brittle yield parameters in SULEC

SULEC assumes a Coulomb yield criterion of the form:

$$\tau_{\max} = p\sin\varphi + c\cos\varphi \tag{E.1}$$

which is derived from the yield on a particular surface, by assuming slip occurs on optimally-oriented planes, and where, p is dynamic pressure (mean stress), c is cohesion and φ is the slope of the failure envelope, i.e., the angle of internal friction (e.g., Ranalli, 1987, p. 95).

If we set $\varphi = 0$ then Eq. (E.1) reduces to the "maximum shear stress criterion" (also known as Tresca criterion):

$$\tau_{max} = c \tag{E.2}$$

Therefore, for the experiments performed here, where φ is set to zero and the brittle strength is prescribed as a cohesion, the cohesion should be entered as the maximum shear stress in SULEC.

References

Batt, G.E., Braun, J., 1999. The tectonic evolution of the Southern Alps, New Zealand: insights from fully thermally coupled dynamical modelling. Geophysical Journal International 136, 403–420.

Brodie, K.H., Rutter, E.H., 2000. Deformation mechanisms and rheology: why marble is weaker than quartzite. Journal of the Geological Society, London 157, 1093–1096.

Buiter, S.J.H., Huismans, R.S., Beaumont, C., 2008. Dissipation analysis as a guide to mode selection during crustal extension and implications for the styles of sedimentary basins. Journal of Geophysical Research 113, B06406.

Cooper, A.F., 1980. Retrograde Alteration of Chromian Kyanite in Metachert and amphibolite Whiteschist from the Southern Alps, New Zealand, with implications for uplift on the Alpine fault. Contribution to Mineralogy and Petrology 75, 153–164.

Cox, S.C., Barrell, D.J.A., 2007. Geology of the Aoraki Area: Scale 1:250,000. In: Institute of Geological and Nuclear Sciences 1:250,000 Geological Map, vol. 15, 71 pp. + 1 folded map.

De Mets, C., Gordon, R.G., Argus, D.F., Stein, S., 1990. Current plate motions. Geophysical Journal International 101, 425–478.

De Mets, C., Gordon, R.G., Argus, D.F., Stein, S., 1994. Effect of recent revisions to the geomagnetic reversal time scale on estimates of current plate motions. Geophysical Research Letters 21, 2191–2194.

Dunlap, W.J., Hirth, G., Teyssier, C., 1997. Thermomechanical evolution of a ductile duplex. Tectonics 16 (6), 983–1000.

Fullsack, P., 1995. An arbitrary Lagrangian-Eulerian formulation for creeping flows and its application in tectonic models. Geophysical Journal International 120, 1–23.

Fusseis, F., Handy, M.R., Schrank, C., 2006. Networking of shear zones at the brittle-to-viscous transition (Cap de Creus, NE Spain). Journal of Structural Geology 28, 1228–1234.

Gleason, G.C., Tullis, J., 1995. A flow law for dislocation creep of quartz aggregates determined with the molten salt cell. Tectonophysics 247, 1–23.

Grapes, R., Watanabe, T., 1992. Metamorphism and uplift of Alpine schist in the Franz Josef-Fox Glacier area of the Southern Alps, new-Zealand. Journal of Metamorphic Geology 10 (2), 171–180.

Gratier, J.P., Gamond, J.F., 1990. Transition between Seismic and Aseismic Deformation in the Upper Crust. Geological Society, London. Special Publications 54, 461–473.

Grigull, S. 2011. Insights into the rheology of rocks under brittle-ductile deformation conditions from an exhumed shear array in the Southern Alps, New Zealand. Unpublished PhD thesis, Victoria University of Wellington.

Grigull, S., Little, T.A., 2008. A graphical-algebraic method for analysing shear zone displacements from observations on arbitrarily oriented outcrop surfaces. Journal of Structural Geology 30, 868–875.

Hill, M.P. 2005. Evolution of quartz and calcite microstructures exhumed from deep brittle-ductile shear zones in the Southern Alps of New Zealand. Unpublished MSc thesis, Victoria University of Wellington.

Hirth, G., Teyssier, C., Dunlap, W.J., 2001. An evaluation of quartzite flow laws based on comparisons between experimentally and naturally deformed rocks. International Journal of Earth Sciences (Geologische Rundschau) 90, 77–87.

Hirth, G., Tullis, J., 1992. Dislocation creep regimes in quartz aggregates. Journal of Structural Geology 14 (2), 145–159.

Hirth, G., Tullis, J., 1994. The brittle-plastic transition in experimentally deformed quartz aggregates. Journal of Geophysical Research 99 (B6), 11731–11747.

Hudleston, P.J., Lan, L., 1993. Information from fold shapes. Journal of Structural Geology 15 (3–5), 253–264.

Hudleston, P.J., Lan, L., 1994. Rheological controls on the shapes of single-layer folds. Journal of Structural Geology 16 (7), 1007–1021.

Hudleston, P.J., Lan, L., 1995. Rheological information from geological structures. Pure and Applied Geophysics 145 (3/4), 605–620.

Huismans, R.S., Buiter, S.J.H., Beaumont, C., 2005. Effect of plastic-viscous layering and strain softening on mode selection during lithospheric extension. Journal of Geophysical Research 110 (B02406), 17.

Kenis, I., Urai, J.L., van der Zee, W., Sintubin, M., 2004. Mullions in the High-Ardenne Slate Belt (Belgium): numerical model and parameter sensitivity analysis. Journal of Structural Geology 26, 1677–1692.

Kenis, I., Urai, J.L., van der Zee, W., Hilgers, C., Sintubin, M., 2005. Rheology of fine-grained siliciclastic rocks in the middle crust - evidence from structural an numerical analysis. Earth and Planetary Science Letters 233, 351–360.

Kleffmann, S., Davey, F., Melhuish, A., Okaya, D., Stern, T., Team, S., 1998. Crustal structure in the central South Island, New Zealand, from the Lake Pukaki seismic experiment. New Zealand Journal of Geology and Geophysics 41 (1), 39–49.

Lan, L., Hudleston, P.J., 1995a. The effects of rheology on the strain distribution in single layer buckle folds. Journal of Structural Geology 17 (5), 727–738.

Lan, L., Hudleston, P.J., 1995b. A method of estimating the stress exponent in the flow law for rocks using fold shape. Pure and Applied Geophysics 145 (3–4), 605–620.

Lan, L., Hudleston, P.J., 1996. Rock rheology and sharpness of folds in single layers. Journal of Structural Geology 18 (7), 925–931.

Leitner, B., Eberhart-Phillips, D., Anderson, H., Nabelek, J.L., 2001. A focused look at the Alpine fault, New Zealand: seismicity, focal mechanisms, and stress observations. Journal of Geophysical Research 106 (B2), 2193–2220.

Lister, G.S., Baldwin, S.L., 1996. Modelling the effect of arbitrary P-T-t histories on argon diffusion in minerals using the Mac Argon program for the Apple Macintosh. Tectonophysics 253, 83–109.

Little, T.A., 2004. Transpressive ductile flow and oblique ramping of lower crust in a two-sided orogen: insight from quartz grain-shape fabrics near the Alpine fault, New Zealand. Tectonics 23 (TC2013).

Little, T.A., Holcombe, R.J., Ilg, B.R., 2002a. Ductile fabrics in the zone of active oblique convergence near the Alpine Fault, New Zealand: identifying the neotectonic overprint. Journal of Structural Geology 24 (1), 193–217.

Little, T.A., Holcombe, R.J., Ilg, B.R., 2002b. Kinematics of oblique collision and ramping inferred from microstructures and strain in middle crustal rocks, central Southern Alps, New Zealand. Journal of Structural Geology 24 (1), 219–239.

Little, T.A., Wightman, R., Holcombe, R.J., Hill, M.P., 2007. Transpression models and ductile deformation of the lower crust of the Pacific Plate in the central Southern Alps, a perspective from field geology. In: Okaya, D., Stern, T., Davey, F. (Eds.), A Continental Plate Boundary – Tectonics at South Island, New Zealand. Geophysical Monograph, vol. 175. American Geophysical Union, Washington, D.C, pp. 271–288.

Luan, F.C., Paterson, M.S., 1992. Preparation and deformation of synthetic aggregates of quartz. Journal of Geophysical Research 97 (B1), 301–320.

Malvern, L.E., 1969. Introduction to the Mechanics of a Continuous Medium. Prentice-Hall, Inc., Englewood Cliffs, New Jersey.

Mancktelow, N.S., Pennacchioni, G., 2005. The control of precursor brittle fracture and fluid-rock interaction on the development of single and paired ductile shear zones. Journal of Structural Geology 27, 645–661.

Mercier, J.C.C., Anderson, D.A., Carter, N.L., 1977. Stress in the lithosphere. Inferences from steady state flow of rocks. Pure and Applied Geophysics 115, 199–226.

Moresi, L., Dufour, F., Muehlhaus, H.-B., 2003. A Lagrangian integration point finite element method for large deformation modeling of viscoelastic geomaterials. Journal of Computational Physics 184, 476–497.

Norris, R.J., Cooper, A.F., 1995. Origin of small-scale Segmentation and Transpressional Thrusting along the Alpine fault, new-Zealand. Geological Society of America Bulletin 107 (2), 231–240.

Norris, R.J., Cooper, A.F., 2001. Late Quarternary slip rates and slip partitioning on the Alpine fault, New Zealand. Journal of Structural Geology 23, 507–520.

Norris, R.J., Cooper, A.F., 2003. Very high strains recorded in mylonites along the Alpine Fault, New Zealand: implications for the deep structure of plate boundary faults. Journal of Structural Geology 25, 2141–2157.

Norris, R.J., Cooper, A.F., 2007. The Alpine fault, New Zealand: surface geology and field relationships. In: Okaya, D., Stern, T., Davey, F. (Eds.), A Continental Plate Boundary: Tectonics at South Island, New Zealand. Geophysical Monograph, vol. 175. American Geophysical Union, Washington, D.C, pp. 157–174.

Ohlmacher, G.C., Aydin, A., 1997. Mechanics of vein, fault and solution surface formation in the Appalachian Valley and Ridge, northeastern Tennessee, U.S.A.: implications for fault friction, state of stress and fluid pressure. Journal of Structural Geology 19 (7), 927–944.

Paterson, M., Luan, F., 1990. Quartzite rheology under geological conditions. In: Knipe, R., Rutter, E.H. (Eds.), Deformation Mechanisms, Rheology and Tectonics. Geological Society Special Publication, vol. 54. Geological Society of London, pp. 299–307.

Pitzer, K.S., Sterner, S.M., 1994. Equations of state valid continuously from zero to extreme pressures for H_2O and CO_2. Journal of Chemical Physics 101 (4), 6.

Ranalli, G., 1987. Rheology of the Earth. Allen and Unwin, Boston.

Rutter, E.H., Brodie, K.H., 2004a. Experimental grain size-sensitive flow of hot-pressed Brazilian quartz aggregates. Journal of Structural Geology 26, 2011–2023.

Rutter, E.H., Brodie, K.H., 2004b. Experimental intracrystalline plastic flow in hot-pressed synthetic quartzite prepared from Brazilian quartz crystals. Journal of Structural Geology 26, 259–270.

Scherwath, M., Stern, T., Davey, F., Okaya, D., Holbrook, W.S., Davies, R., Kleffmann, S., 2003. Lithospheric structure across oblique continental collision in New Zealand from wide-angle P wave modeling. Journal of Geophysical Research 108 (B12), 2566.

Scholz, C.H., 1988. The brittle-plastic transition and the depth of seismic faulting. International Journal of Earth Sciences (Geologische Rundschau) 77 (1), 319–328.

Schueller, S., Gueydan, F., Davy, P., 2005. Brittle-ductile coupling: role of ductile viscosity on brittle fracturing. Geophysical Research Letters 32, L10308.

Schueller, S., Gueydan, F., Davy, P., 2010. Mechanics of the transition from localized to distributed fracturing in layered brittle-ductile systems. Tectonophysics 484 (1–4), 48–59.

Shi, Y., Allis, R., Davey, F., 1996. Thermal modeling of the Southern Alps, New Zealand. Pure and Applied Geophysics 146 (3–4), 469–501.

Stern, T., Kleffmann, S., Okaya, D., Scherwath, M., Bannister, S., 2001. Low seismic-wave speeds and enhanced fluid pressure beneath the Southern Alps of New Zealand. Geology 29 (8), 679–682.

Stern, T., Okaya, D., Kleffmann, S., Scherwath, M., Henrys, S., Davey, F., 2007. Geophysical Exploration and dynamics of the Alpine fault zone. In: Okaya, D., Stern, T., Davey, F. (Eds.), A Continental Plate Boundary – Tectonics at South Island, New Zealand. Geophysical Monograph, vol. 175. American Geophysical Union, Washington, D.C, pp. 207–232.

Stipp, M., Tullis, J., 2003. The recrystallized grain size piezometer for quartz. Geophysical Research Letters 30 (21), 1–5. SDE 3.

Stöckhert, B., Brix, M.R., Kleinschrodt, R., Hurford, A.J., Wirth, R., 1999. Thermochronometry and microstructures of quartz - a comparison with experimental flow laws and predictions on the temperature of the brittle-plastic transition. Journal of Structural Geology 21, 351–369.

Sutherland, R., Berryman, K., Norris, R., 2006. Quaternary slip rate and geomorphology of the Alpine fault: implications for kinematics and seismic hazard in southwest New Zealand. Geological Society of America Bulletin 118 (3–4), 464–474.

Talbot, C.J., 1999. Ductile shear zones as counterflow boundaries in pseudoplastic fluids. Journal of Structural Geology 21, 1535–1551.

Talbot, C.J., 2001. Ductile shear zones as counterflow boundaries in pseudoplastic fluids: reply. Journal of Structural Geology 23, 157–159.

Thomas, J.B., Watson, E.B., Spear, F.S., Shemella, P.T., Nayak, S.K., Lanzirotti, A., 2010. TitaniQ under pressure: the effect of pressure and temperature on the solubility of Ti in quartz. Contribution to Mineralogy and Petrology 160, 743–759.

Toy, V.G., 2007. Rheology of the Alpine Fault mylonite zone: deformation processes at and below the base of the seismogenic zone in a major plate boundary structure. Unpublished PhD thesis, University of Otago.

Toy, V.G., Prior, D.J., Norris, R.J., 2008. Quartz fabrics in the Alpine Fault mylonites: influence of pre-existing preferred orientations on fabric development during progressive uplift. Journal of Structural Geology 30 (5), 602–621.

Treagus, S.H., 1999. Are viscosity ratios of rocks measurable from cleavage refraction? Journal of Structural Geology 21, 895–901.

Treagus, S.H., Hudleston, P.J., Lan, L., 1996. Non-ellipsoidal inclusions as geological strain markers and competence indicators. Journal of Structural Geology 18 (9), 1167–1172.

Treagus, S.H., Lan, L., 2000. Pure shear deformation of square objects, and applications to geological strain analysis. Journal of Structural Geology 22 (1), 105–122.

Treagus, S.H., Lan, L., 2003. Simple shear of deformable square objects. Journal of Structural Geology 25 (12), 1993–2003.

Treagus, S.H., Lan, L., 2004. Deformation of square objects and boudins. Journal of Structural Geology 26, 1361–1376.

Treagus, S.H., Treagus, J.E., 2002. Studies of strain and rheology of conglomerates. Journal of Structural Geology 24, 1541–1567.

Tullis, J., Yund, R.E., 1982. Grain growth kinetics of quartz and calcite aggregates. Journal of Geology 90 (3), 301–318.

Vry, J.K., Baker, J., Maas, R., Little, T.A., Grapes, R., Dixon, M., 2004. Zoned (Cretaceous and Cenozoic) garnet and the timing of high grade metamorphism, Southern Alps, New Zealand. Journal of Metamorphic Geology 22 (3), 137–157.

Vry, J.K., Powell, R., Golden, K.M., Petersen, K., 2010. The role of exhumation in metamorphic dehydration and fluid production. Nature Geoscience 3, 31–35.

Wannamaker, P.E., Jiracek, G.R., Stodt, J.A., Caldwell, T.G., Gonzalez, V.M., McKnight, J.D., Porter, A.D., 2002. Fluid generation and pathways beneath an active compressional orogen, the New Zealand Southern Alps, inferred from magnetotelluric data. Journal of Geophysical Research 107 (B6), 20.

Wark, D.A., Watson, E.B., 2006. TitaniQ: a titanium-in-quartz geothermometer. Contribution to Mineralogy and Petrology 152, 743–754.

Wightman, R., 2005. Deformation and Orogenesis: the Geodynamic Significance of a Brittle-Ductile Fault Array in the Central Southern Alps, New Zealand. Unpublished PhD thesis, Victoria University of Wellington.

Wightman, R., Little, T.A., 2007. Deformation of the Pacific Plate above the Alpine Fault ramp and its relationship to expulsion of metamorphic fluids: an array of backshears. Geophysical Monograph Series AGU 175, 177–205.

Wightman, R., Prior, D.J., Little, T.A., 2006. Quartz veins deformed by diffusion creep-accomodated grain boundary sliding during a transient, high strain-rate event in the Southern Alps, New Zealand. Journal of Structural Geology 28, 902–918.